2015

Exciton Dynamics in Rubrene Single Crystals

Kebra Ann Ward
Lehigh University

Recommended Citation

Ward, Kebra Ann, "Exciton Dynamics in Rubrene Single Crystals" (2015). *Theses and Dissertations*. 2870.
http://preserve.lehigh.edu/etd/2870

Exciton Dynamics in Rubrene Single Crystals

by

Kebra Ann Ward

A Dissertation
Presented to the Graduate Committee
of Lehigh University
in Candidacy for the Degree of
Doctor of Philosophy
in
Physics

Lehigh University
August 2015

Approved and recommended for acceptance as a dissertation in partial fulfillment of the requirements for the degree of Doctor of Philosophy.

Kebra Ann Ward
Exciton Dynamics in Rubrene Single Crystals

Date

Ivan Biaggio, Dissertation Director, Chair

Accepted Date

Committee Members

John Huennekens

Vyacheslav V. Rotkin

Michael J. Stavola

Nicholas Strandwitz

For Daniel, my most favorite, who kept me alive and fed throughout all of this insanity.

&

For my mother, who supplied all the H_2O I've ever needed.

Contents

List of Tables

List of Figures

Abstract

In this work, transient grating pump and probe experiments are used to investigate excitonic processes in the rubrene single crystal. Rubrene is a high quality organic crystal with particularly intriguing material properties that make it interesting for the study of various physical processes of importance for optoelectronics.

On the nanosecond time scale we find that bimolecular interactions cause a photoinduced excited state density on the order of $\sim 0.5 \times 10^{20}$ cm^{-3} — corresponding to an average distance of $\sim$ 3 nm between individual states — to decrease by a factor of two after 2 ns, following a typical power-law decay. We assign the observed power-law decays to high-density interactions between excited states. Because of the high efficiency singlet exciton fission observed in rubrene, these bimolecular interactions are likely those between triplet excitons or a singlet exciton and a pair of triplet excitons in a coherent quantum superposition.

Transient grating experiments performed on the picosecond time scale are then used to track the build-up of the photoinduced excited state. The build up to a quasi steady-state amplitude of the grating within 10 ps is consistent with the affirmation that the build-up tracks the creation of triplet states by singlet fission, which then implies the bimolecular interactions seen on the nanosecond time scale are indeed those of triplets or the coherent quantum superposition of a singlet and a pair or triplet excitons.

Lastly we use the transient grating techniques in a spectroscopic capacity in order to track how the observed grating dynamics and the exciton dynamics that can be inferred from it depend on the energy of the photons used for excitation, which determine the initial excitation energy deposited in the material and the

vibrational mode of the excited state. We find that the time it takes to create triplet excitons by fission increases with increasing excitation energy, and once an excitation threshold of $\sim$ 2.7 eV is passed, corresponding to approximately the third vibronic resonance of the singlet state, we loose the ability to track the triplet population in our experiment.

Chapter 1

Introduction

The physics of energy dynamics in organic molecular crystals is an appealing area of study due to the prospect of developing organics for use in optoelectronic devices. This dissertation will present the results of pulsed laser light creating an excitation in an organic molecular crystal, and how that excitation evolves over time.

Molecular crystals bound via van der Waals forces have several unique properties. Van der Waals forces are significantly weaker than covalent bonds, and therefore molecular crystals are characterized by flat valence and conduction bands that result in low charge mobility. They have high exciton binding energies, up to ∼1.5 eV [1], allowing excitonic effects to dominate the optical response at room temperature and making it hard for excitons to dissociate into free carriers.

Some organic crystals find themselves in a class of molecular crystals that exhibit semiconductor-like characteristics. For this reason there has recently been great focus on researching organic crystals, as organic materials are poised for development in optoelectronic devices such as organic photovoltaics (PV) [2–5], organic light emitting diodes (OLED) [6, 7], and organic field effect transistors (OFETS) [8, 9].

Before that development can most efficiently be done, energy transport in organic crystals must be properly understood. As an example, the ability to develop organics for use in photovoltaic devices relies on the creation of many excitons that can then dissociate into free carriers. Singlet fission, where an excited state singlet spontaneously splits into two triplets states, exhibits much potential to create a large population of excitons with a long diffusion length after photoexcitation.

This dissertation will present studies into the inter-molecular interactions that occur during exciton fission with the intent to develop a better fundamental picture of singlet and triplet interactions in organic molecular crystals. This will be accomplished by investigating the physical mechanisms of exciton dynamics in single-crystal rubrene via pump and probe experiments.

Rubrene is an anisotropic, single-crystal organic molecular material. This crystal is of interest for fundamental study due to its long triplet exciton diffusion length and relatively high hole mobility compared to other organic materials. These traits provide the opportunity to study transport in a high-quality, ordered molecular system. The results obtained by studying rubrene can then be applied to other ordered systems for use in developing opto-electronic devices such as organic photovoltaic cells.

The focus of this work will be on the creation of triplet excitons via singlet fission, and how those triplets interact once created. The singlet fission process has been shown to be very efficient in rubrene, therefore leading to a large population of triplets after pulsed photoexcitation. The mechanisms that govern singlet fission are not well known, with lots of conflicting data and interpretations in the literature. We intend to clear up some of the confusion.

We will investigate exciton dynamics by use of pulsed, wavelength tunable lasers to perform pump and probe transient grating experiments. Transient grating experiments are based on the photoexcitation of a spatial excited state distribution. These experiments use the interference pattern between two optical pulses, followed by the detection of the resulting absorption or polarizability changes by diffraction of a time-delayed probe pulse from the resulting grating. Compared to the straight detection of a photoinduced absorption, transient grating experiments are characterized by a backgroundless signal that allows the detection of both absorption and refractive index changes with a higher sensitivity.

In Chapter 2 we will detail the experimental techniques used in this work and what may be detected by these techniques. Chapter 3 will present a review of molecular crystals and the fission process, in addition to describing the rubrene single crystal. Chapter 4 will discuss transient grating dynamics in rubrene on a nanosecond time scale. Chapter 5 will present transient grating experiments on the picosecond time scale that, among other things, confirm our assignment of the excited state studied in Chapter 4. Chapter 6 will review the evolution of the transient grating response observed on the picosecond time scale as the wavelength of the excitation and detection light is varied, and the spectroscopic insights that can be gained from it.

Chapter 2

Pump & Probe Transient Gratings

The interaction of light and matter can produce amazing photo-physical results. Plants use absorbed sunlight to convert water and carbon dioxide into glucose in order to produce their own food. When ultra-violet light is absorbed by human skin it can damage the skin cell's DNA, resulting in a wicked burning of flesh. The absorption of sunlight by a semiconductor can ultimately result in the flow of electrical current. When light and materials meet, interesting physics is often afoot.

The advent of the laser in 1960 provided the coherent and intense light pulses necessary to better observe light-matter interactions, allowing the study of the time dynamics of electronic processes. With the development in 1965 of lasers that could generate short, picosecond pulses, experiments could be performed where a sample is excited by one short pulses (the pump), then another pulse passes through or is reflected from the surface of the sample (the probe). For this reason, these types of experiments are often referred to as 'Pump & Probe'. Delaying the probe pulse allows the excitation to be monitored as it evolves in time. The pulse width ultimately determines the time resolution with which these processes can be monitored.

The use of pulsed lasers allows for the observation of fast dynamics inaccessible via other methods. Physical processes associated with the creation of excitons in molecular crystals and the transfer of energy thereafter are an example of phenomena whose study can benefit from such high time resolution.

A pulse of light can locally (in that spot where the light is) change the material properties of the sample, for example the complex index of refraction of the material. When a probe pulse then passes through the region of modulated complex index of refraction, the probe pulse will be altered in some way; it will either undergo a phase shift if the real part is changed (the standard interpretation of index of refraction) or absorbed differently if the imaginary part is changed.

It is possible to spatially modulate the excitation caused by the pump by using two pump pulses that interfere. The resulting interference pattern will create alternating regions of high and low intensity light. Since material properties such as the complex index of refraction are altered by the light intensity, the alternating intensity will produce a periodic modulation of the complex refractive index. Arranging the propagation direction of the probe pulse to be at the Bragg angle allows one to detect the strength of the grating by detecting of the Bragg diffracted intensity.

By delaying the arrival time of the probe pulse, the time evolution of the diffraction grating may be observed. Transient gratings are a particularly versatile phenomenon. This chapter will discuss the creation of this transient grating via photexcitation as a method for monitoring the time dynamics of molecules brought to an excited state by the absorption of light.

2.1 Creating the Transient Grating: Interference Patterns and Complex Refractive Index

In this work we observe the time dynamics of an excitation by detecting the relaxation of the photoinduced transient grating. The principles of transient gratings lie in the use of the interference pattern between two optical pulses to photoexcite a spatially modulated excited state distribution, followed by the detection of the resulting absorption or polarizability changes by diffraction of a time-delayed probe pulse from the grating.

To create the transient grating, we start with two pulses with wave vectors $\mathbf{k_1}$ and $\mathbf{k_3}$ and electric field amplitudes of $\mathbf{E_1}$ and $\mathbf{E_3}$, respectively, crossing in the bulk of the material. The intensity of each pulse is proportional to the square of its

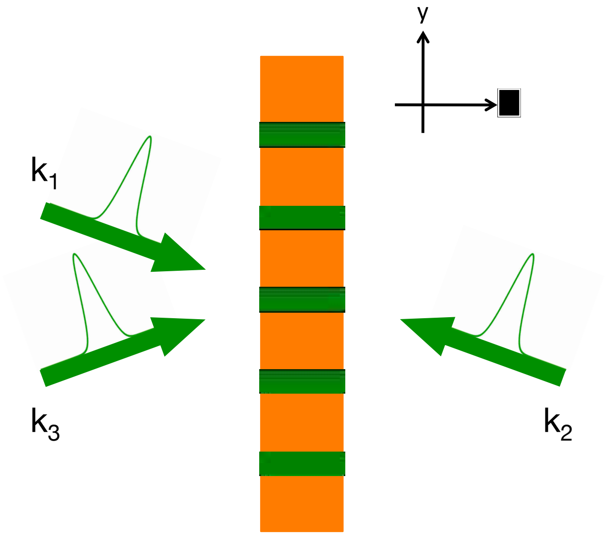

Figure 2.1: Two beams, $\mathbf{k_1}$ and $\mathbf{k_3}$ creating an interference pattern, and counterpropagating beam $\mathbf{k_2}$ passing through to be diffracted.

electric fields, $I_i \propto |\mathbf{E_i}|^2$. When the two pulses interfere they create a sinusoidal interference pattern inside the material.

If we set the grating wavevector along the y-direction, the periodic modulation of the light is described by

$$I = I_0 \left[1 + m_0 \cos(k_g y)\right] \tag{2.1}$$

where $I_0 = I_1 + I_3$ is the sum of the intensities of the two interfering pulses for light polarized perpendicular to the plane of incidence, m_0 is a modulation index given by $2\sqrt{I_1 I_2}/I_0$, and k_g is the modulus of the grating wavevector, which depends on the grating spacing as

$$k_g = \frac{2\pi}{\Lambda}, \tag{2.2}$$

where Λ is the modulation period of the grating, as

$$\Lambda = \frac{\lambda}{2\sin\theta} \tag{2.3}$$

where λ is the wavelength of light and θ is the half angle between the propagation directions of the two interfering pulses.

Fig. 2.1 shows an example of this interference pattern when the two interfering pulses enter the sample from the same surface to create an interference pattern with a wavevector $\mathbf{k_g} = \mathbf{k_3} - \mathbf{k_1}$ along the y-direction.

When an electromagnetic wave propagates inside a material, its velocity is effected. The index of refraction determines how the velocity changes, and is defined as the ratio of the vacuum speed of light and that in the medium, $n = \frac{c}{v}$, with the phase velocity being the ratio of the frequency and the wavevector, $v = \frac{\omega}{k}$. As the electromagnetic wave passes through the medium, it can also be attenuated by absorption. The attenuation can be taken into account if we define a complex index of refraction,

$$\tilde{n} = n_R + i n_I, \tag{2.4}$$

where n_R is responsible for the change in velocity (simply the n described above) and n_I is responsible for the attenuation.

Consider a plane wave propagating in the y-direction,

$$\vec{\mathbf{E}} = Re\left[\vec{\mathbf{E}}_0 e^{i(ky-\omega t)}\right]. \tag{2.5}$$

If we recast this equation as a function of the complex index of refraction where now $\tilde{n} = \frac{c}{v}$, we obtain, after some arithmetic gymnastics,

$$\vec{\mathbf{E}} = Re\left[\vec{\mathbf{E}}_0 e^{i\omega([\tilde{n}y/c]-t}\right]. \tag{2.6}$$

Substituting $\tilde{n} = n_R + i n_I$ yields

$$\vec{\mathbf{E}} = Re\left[\vec{\mathbf{E}}_0 e^{i\omega([n_R y/c]-t)} \;\; e^{\frac{-\omega n_I}{c} y}\right] \tag{2.7}$$

where the first exponential describes how the wave propagates in the y-direction with velocity c/n_R, and the second exponential term describes how the wave is attenuated as it propagates in the y-direction.

As the intensity of the wave is proportional to the square of its electric field, the intensity for a wave traveling through a medium is therefore attenuated as

$$I(y) = I_0 e^{-2\frac{\omega n_I}{c} y} = I_0 e^{-\alpha y}, \tag{2.8}$$

where $\alpha \equiv 2\frac{\omega n_I}{c}$ is the absorption coefficient.

Light can influence the real and imaginary part of the refractive index as it passes through the medium [10]. This influence is due to the fact that the sample's molecules have been promoted to an excited state, altering the absorption and the permittivity ϵ of the sample. The permittivity is related to the refractive index as $n = \sqrt{\epsilon\mu}$, where μ is the magnetic permeability. Any change to the permittivity will then change the refractive index. Since the light is modulated due to an interference pattern, the permittivity and therefore refractive index are also modulated. This results in the establishment of a diffraction grating in the bulk of the sample created by parallel planes of alternating index of refraction (or coefficient of absorption).

Diffraction will always occur for any change in the index of refraction. The ability to *detect* this change depends on whether the change in refractive index or absorption is large enough. For example in our experiments this detection limit corresponds to $\triangle n = 1 \times 10^{-6}$ for a 1 mm thick sample. For such an index modulation, the amplitude of the diffraction grating and its time-dependence can be determined by diffraction of the time-delayed probe pulse. A portion of the probe pulse will be diverted from its transmitted path, radiating a fourth pulse from inside the bulk of the material; the detected signal. The period of this modulation may be altered by adjusting the crossing angle (θ in Eqn. 2.3) for the pump pulses.

2.2 Experimental Geometries

Once the transient grating is established, the passage of a probe beam with wavevector $\mathbf{k_2}$ (see Fig. 2.1) through the grating will result in the radiation of the signal pulse in thick samples as long as the probe pulse satisfies the Bragg condition. The Bragg condition requires phase matching between the radiated signal $\mathbf{k_4}$ and the input beams, and is achieved when $\mathbf{k}_4 = \mathbf{k}_1 + \mathbf{k}_2 - \mathbf{k}_3$. Any radiation that does not match the Bragg condition will not be diffracted by a thick grating. Diffraction from a thin grating is possible, and will be addressed in section 2.4.

There are two practical geometric configurations that ensure phase matching and

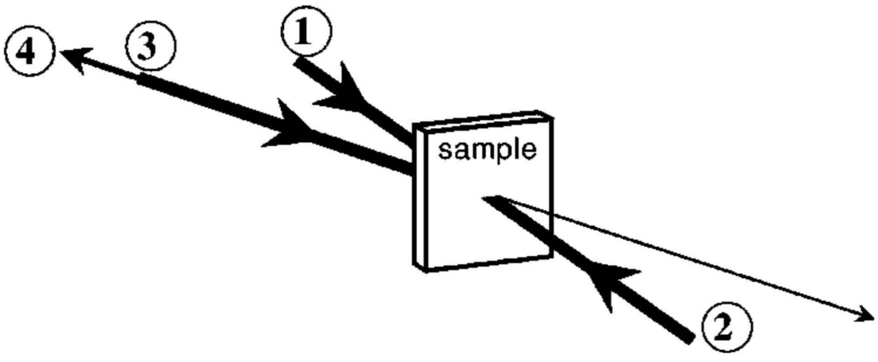

Figure 2.2: Phase Conjugate configuration used to achieve phase matching in the Bragg condition [11]. Beams $\mathbf{k_1}$ and $\mathbf{k_3}$ are the pump beams that interfere to create the transient grating. The probe beam $\mathbf{k_2}$ travels counterpropogating to $\mathbf{k_1}$ and is diffracted. Beam $\mathbf{k_4}$ is the detected beam that travels counterpropagating to $\mathbf{k_3}$.

that the Bragg condition is met: phase conjugate and forward facing.

In the phase conjugate configuration, the pump beams $\mathbf{k_1}$ and $\mathbf{k_3}$ enter the sample from the plane of incidence at one surface of the sample, while the probe beam $\mathbf{k_2}$ enters the sample in the plane of incidence from the other surface. To satisfy the Bragg condition, $\mathbf{k_2}$ must be counterpropagating to $\mathbf{k_1}$. Fig. 2.2 from Ref. [11] shows the necessary geometry at the surface of the sample.

In the forward facing configuration, all three beams are incident at the same surface of the sample. This geometry requires that the two pump beams $\mathbf{k_1}$ and $\mathbf{k_3}$ propagate through two corners a square while the probe beam $\mathbf{k_2}$ passes through a third corner to ensure the Bragg condition. Fig. 2.3 from Ref. [11] shows the proper location of each beam. In this scenario, the radiated signal beam $\mathbf{k_4}$ must then propagate such that it passes through the fourth, empty corner of the square.

An interesting aspect of the forward facing configuration is the ability to see additional radiated waves due to other, non-Bragg matched diffraction processes when the grating is thin enough. In Fig. 2.4 the smaller green circles represent the diffraction due to three interacting beams. The $\mathbf{k_4}$ beam that completes the square

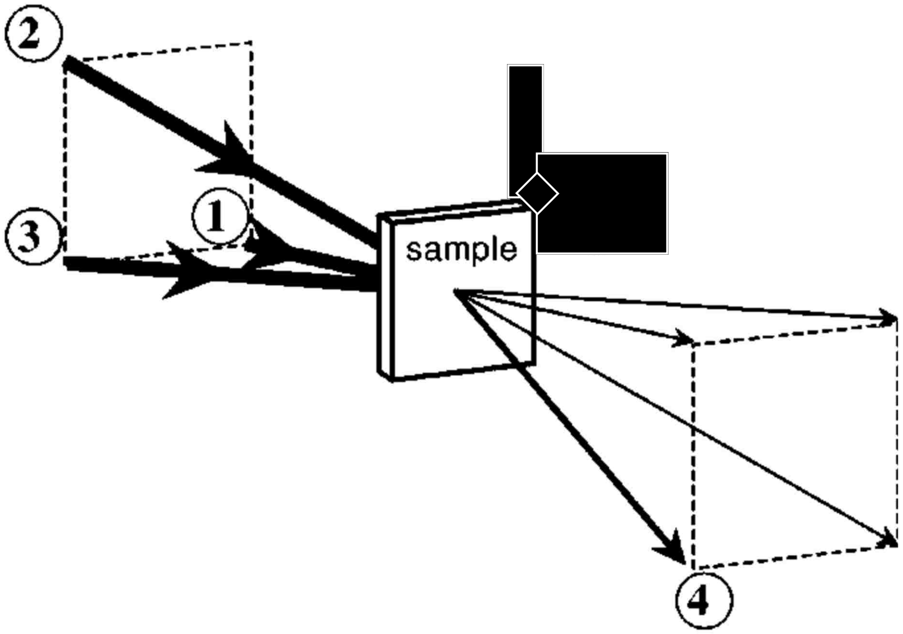

Figure 2.3: Forward facing configuration used to achieve phase matching in the Bragg condition [11]. Beams $\mathbf{k_1}$ and $\mathbf{k_3}$ are the pump beams that interfere to create the transient grating. Beam $\mathbf{k_2}$ is the probe beam. The three beams propagate such that their wavevectors pass through three corners of a square at all times. The radiated beam $\mathbf{k_4}$ passes through the fourth corner of the square.

is the phase matched beam that results from first order Bragg diffraction from the transient grating. The other two $\mathbf{k_4}$ beams are from the non-phase-matched first order Raman-Nath diffraction (see section 2.4), and the blue squares are signals from two-beam self diffraction. The blue squares can occur before, at, and after time zero, depending on which of the two light pulses arrive at the same time in the sample.

In this work the phase conjugate set-up will be used to do long time scans of the decay of the transient grating, which will be discussed in Chapter 4. The forward facing set-up will be used to monitor the build-up of the transient grating by doing shorter scans with a smaller time resolution than that of the phase conjugate set-up, with discussions following in Chapters 5 and 6. The long and short scans are

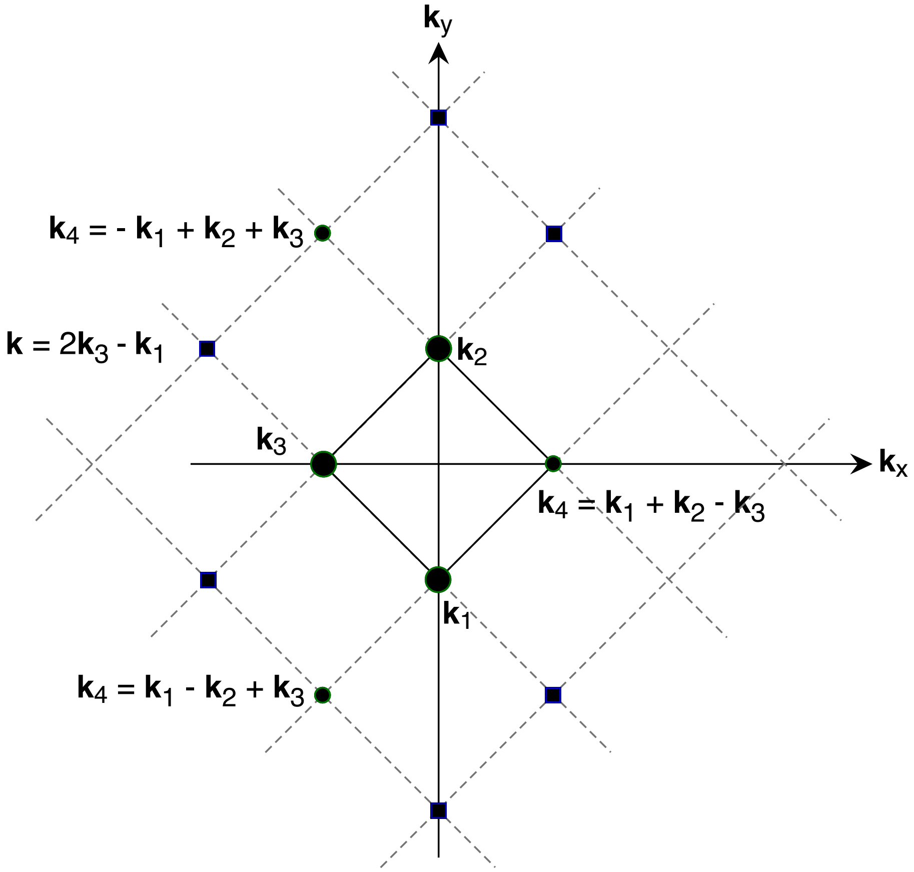

Figure 2.4: Graphical representation of the wavevector coordinates of the interacting beams. The small green circles, indicated by $\mathbf{k_4}$ are the waves radiated by Bragg and Raman-Nath diffraction. The wave $\mathbf{k_4}$ lying on the k_x axis is the detected signal. The blue squares represent waves radiated due to other diffraction processes.

possible due to the two different lasers operating in each experimental set -up.

2.3 Description of the Experimental Set-Ups

In the phase conjugate configuration, the generated second harmonic pulse ($\lambda =$ 532nm) from an Ekspla PL2143B Nd:Yag pulsed laser operating at 10 Hz with a pulse length of $\sim$ 20 ps and maximum output of $\sim$ 20 mJ is used. The output pulse is sent through two beam splitters to produce the three input pulses. The path of

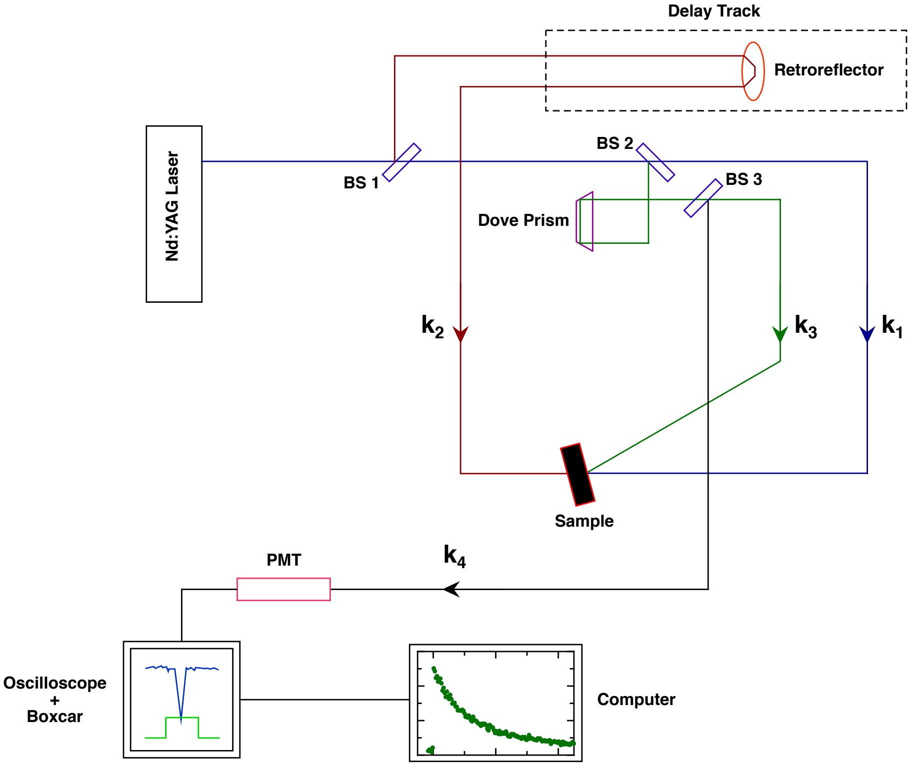

Figure 2.5: Phase conjugate experimental set-up.

the probe pulse involves a Newport retroreflector mounted on an OWiS motorized track that can increase the path length of the probe by 3 m relative to the fixed excitation pulses. This distance allows the arrival time of the probe pulse to be delayed up to 10 ns after the creation of the transient grating. The phase conjugate set-up has the benefit that the crossing angle of the two pump pulses can easily be changed by moving only the path of $\mathbf{k_3}$, see Fig. 2.5.

The importance of the retroreflector can not be stressed enough. A retroreflector is a device that reflects a beam exactly parallel to but in the opposite direction of the incident beam. They can be seen in everyday use in reflective roadsigns. Very precise alignment of the pulse paths is essential to obtaining reliable results from a transient grating experiment. To ensure that the beam does not move while the motorized track increases the delay, it is imperative that the probe beam arrive at the retroreflector *parallel* to the direction in which the motorized track moves. As stated above, any deviation of the pulse from the path required by the Bragg condition would result in a loss of signal. More importantly, slight changes in the position of the probed spot could affect the experimental results. In the most extreme case, if the probe were to move to a spot that does not contain any grating while the timing is being changed, the signal would be completely lost. The probe pulse becomes very susceptible to deviations as its delay is increased by the motorized track.

Inhomogeneities in some sample's structure have the potential to produce a great amount of scattering if the probe pulse's path is deviated even slightly, which would obscure detection of the radiated signal pulse. Use of the retroreflector ensures that the location of the probe pulse inside the sample does not deviate from the area defined by the transient grating, therefore minimizing the possibility of any deviation from the required path as the delay line for the probe is increased, allowing an accurate detection of our radiated signal.

The path of one of the excitation pulses involves a mounted dove prism to make precision adjustments to its path length to guarantee it arrives completely time coincident with the other excitation pulse. The two excitation pulses arrive at one interface of the sample with their bisectrix parallel to the normal of the sample. The probe pulse arrives at the sample on the other side of the crystal, counterpropagating to one of the excitation pulses, while the generated signal pulse travels counterpropagating to the other excitation pulse. This makes it quite easy to find the radiated signal, since it will propagate exactly counter to one of the pump beams. A beam splitter needs only to be placed along the path of the signal to redirect it towards a photomultiplier tube. This photomultiplier tube is coupled to an oscilloscope and a boxcar integrator that is connected to a computer to record the signal amplitude as a function of time.

In the forward facing configuration, the output of a Clark MXR Ti:Sapphire pulsed laser operating at 1 kHz with a pulse of a full width at half maximum ($FWHM$) of $\sim$ 1ps. This output pumps a Light Conversions Traveling Wave Optical Parametric Amplifier System (TOPAS), which allows the wavelength of the pulse to be tuned between 0.4 μm and 3 μm. Once the desired wavelength has been selected, the pulse is then sent through two beam splitters to create the three input pulses.

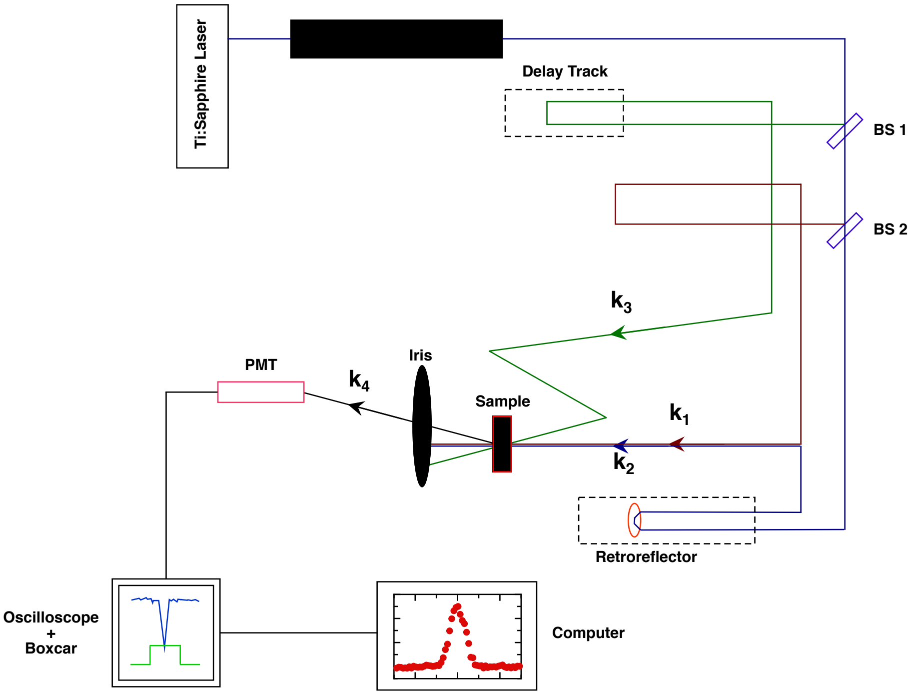

Figure 2.6: Forward facing experimental set-up.

One of the excitation pulses goes through a translational stage to again ensure it arrives completely time coincident with the other excitation pulse, and the probe beam is sent to a ThorLabs retroreflector mounted on a Zaber motorized track to control the arrival time at the sample. The length of this track allowed for a delay of up to 200 ps after creation of the transient grating, compared to the 10 ns delay allowed by the phase conjugate set-up. Fig. 2.6 shows the complete experimental set-up.

The configuration in the forward facing set-up results in the detected signal traveling in the same general direction as the transmitted pump and probe pulses. Therefore the signal pulse must be isolated and directed to a photomultiplier tube that is again connected to an oscilloscope and boxcar integrator connected to a computer that monitors the time dependence of the signal amplitude.

In the forward facing set-up it is much more complicated to alter the crossing angle of the pump pulses. We therefore keep the angle fixed for measurements in this configuration. A very big advantage of the laser system used in this set-up is that it incorporates the TOPAS optical parametric amplifier, and thus has the benefit of allowing experiments to be performed at different wavelengths, which is not possible in our phase conjugate set-up.

2.4 Detected Responses

While the pump pulses are incident on the sample, they are exciting the molecules. The amplitude of the detected signal versus the time delay of the probe pulse can tell us much about the mechanisms of that excitation. It may present as an instantaneous peak if the response happens on a time scale much shorter than the pulse length. It could appear as a step from energy being deposited within the lifetime of the pulse. If a process takes much longer than the lifetime of the pulse we would be able to observe, for example, the exponential build-up or decay of a state. These types of responses will be discussed in the next few sections.

2.4.1 Degenerate Four Wave Mixing: The Instantaneous Response

When the probe pulse being diffracted by the grating has the same frequency as the two excitation pulses, the coupling of these three input pulses results in the creation of a fourth pulse of equal frequency. When the response of the system happens much quicker than the pulse length, the diffracted signal will build to a maximum at time t = 0 ps and then relaxes again in a time related to the *FWHM* of the laser pulse. This instantaneous process is called degenerate four wave mixing (DFWM). It is a third order nonlinear process because there are three input pulses and nonlinear because it depends on the nonlinear susceptibility, $\chi^{(3)}_{ijkl}$, as it appears in the complex amplitude of the induced polarization.

$$\mathcal{P}_i^{(3)}(\omega, \mathbf{k_4}) = \frac{3}{2}\epsilon_0 \chi^{(3)}_{ijkl}(-\omega, -\omega, \omega, \omega, -\mathbf{k_4}, \mathbf{k_3}, \mathbf{k_2}, \mathbf{k_1})\mathcal{E}_j(-\omega, -\mathbf{k_3})\mathcal{E}_k(\omega, \mathbf{k_2})\mathcal{E}_l(\omega, \mathbf{k_1}) \tag{2.9}$$

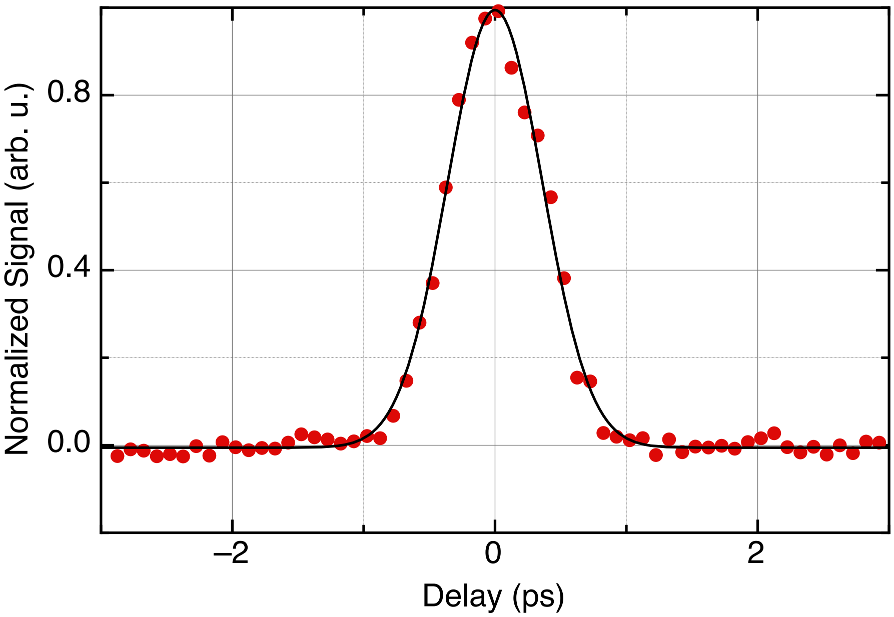

Figure 2.7: Instantaneous non-linear response in a sample of $Bi_{12}GeO_{20}$ taken at 460 nm using the forward facing configuration. The signal reaches a maximum at a delay of $t_{02} = 0$ ps for the probe pulse. The solid line is a Gaussian fit to the data with a time constant of $\tau_{Inst} = 0.72$ ps, corresponding to a *FWHM* for the laser pulses that create the signal of 0.98 ps.

Fig. 2.7 shows a typical result from a DFWM experiment. Note that the signal begins to grow as the probe pulse delay approaches zero, and achieves peak amplitude at a delay of t = 0 ps, indicating that all three input beams are temporally overlapped.

Fig. 2.8 represents three Gaussian pump pulses overlapping in time. The overlap of the probe pulse with the already time coincident pump pulses is responsible for the the signal we detect. When the probe just begins to overlap the pump pulses, the signal starts appearing, and then as the probe is completely synchronized with the pumps, the signal reaches its maximum. Then as the pump delay time increases to greater than zero, the probe arrives after the the pump pulses and the signal decreases. The resulting signal is itself in the form of a Gaussian, $\sim e^{-(t/\tau)^2}$.

The intensity of the generated signal is proportional to the intensities of the

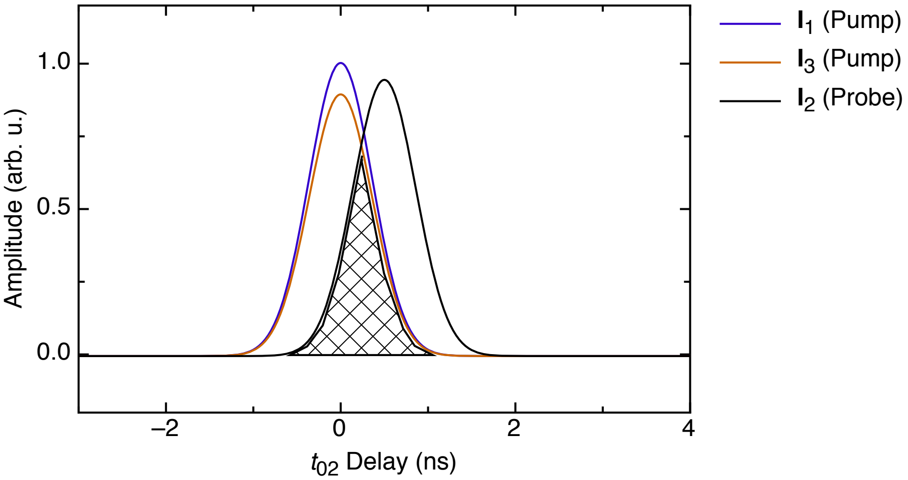

Figure 2.8: Probe pulse arriving at the grating at some delayed time t_{02}. The overlap of the three pulses, marked by the grid, represents the portions of intensity of the three beams that are responsible for the signal energy at t_{02}.

three input beams,

$$I_4(t) \propto I_1(t)I_2(t)I_3(t) = \left[I_1(0)e^{-[(t-t_{01})/\tau]^2}\right]\left[I_2(0)e^{-[(t-t_{02})/\tau]^2}\right]\left[I_3(0)e^{-[(t-t_{03})/\tau]^2}\right], \tag{2.10}$$

where the $I_i(0)$ are the maximum intensities of the pump and pulse beams, the t_{0i} are the delay times of each beam, and τ is the pulse duration as determined by the laser. Since all three beams originate from the same laser, τ is the same for all three beams.

In the transient grating experiments, the pump beams $\mathbf{k_1}$ and $\mathbf{k_3}$ are fixed spatially with complete temporal overlap. We can therefore set $t_{01} = t_{03} = 0$ ps, and integrate over all time to determine the energy of the generated signal.

$$E \propto I_1(0)I_2(0)I_3(0)\int_{-\infty}^{\infty}\left[e^{-(t/\tau)^2}\right]^2 e^{-[(t-t_{02})/\tau]^2}dt \tag{2.11}$$

$$E \propto I_1(0)I_2(0)I_3(0)\sqrt{\frac{\pi}{3}}\tau e^{-\frac{2}{3}(t_{02}/\tau)^2} \tag{2.12}$$

where we see that the energy of the radiated signal varies as a function of t_{02}, the delay time of the probe beam as controlled by the motorized track.

The time constant τ that appears in Eqns. 2.10, 2.11 and 2.12 gives the duration of the laser pulse. If the Gaussian profile of the laser pulse is fit with an equation in the form of $e^{-(t/\tau)}$ and the Gaussian signal that results from diffraction (see Fig. 2.7) is fit with an equation in the form of

$$y \propto e^{-(t/\tau_{Inst})^2}, \tag{2.13}$$

the resulting time constants are related as

$$\tau = \sqrt{\frac{2}{3}}\tau_{Inst} = 0.8165\tau_{Inst}. \tag{2.14}$$

Since τ and the $FWHM$ of the laser pulse are proportional to each other as $FWHM = 2\tau\sqrt{\ln 2}$, and the same relationship is valid for the $FWHM$ of the data measured in a transient grating scan, then the $FWHM$ of the laser pulse can be related to the $FWHM$ of the detected signal:

$$FWHM_{Pulse} = \sqrt{\frac{2}{3}}FWHM_{Inst}. \tag{2.15}$$

2.4.2 Excited State Decay

In some materials, the modulation of the material properties lasts long after $t = 0$ ps. In these cases we can no longer consider only the instantaneous DFWM response, but must take into account the lifetime of the transient grating that is caused by the photoinduced refractive index or absorption change resulting from a long lived excited state of the molecules. This long lived component is detected by measuring its diffraction efficiency over time, that is, the ratio of the diffracted pulse's amplitude to the amplitude of the incident probe pulse. Kogelnik [12] derived an expression for the diffraction efficiency of a thick holographic gratings as

$$\eta = e^{-2\alpha L}|\sin[LA(t)]|^2, \tag{2.16}$$

where

$$A(t) = \frac{\pi}{\lambda}\Delta n(t) + i\frac{\Delta\alpha(t)}{4}, \tag{2.17}$$

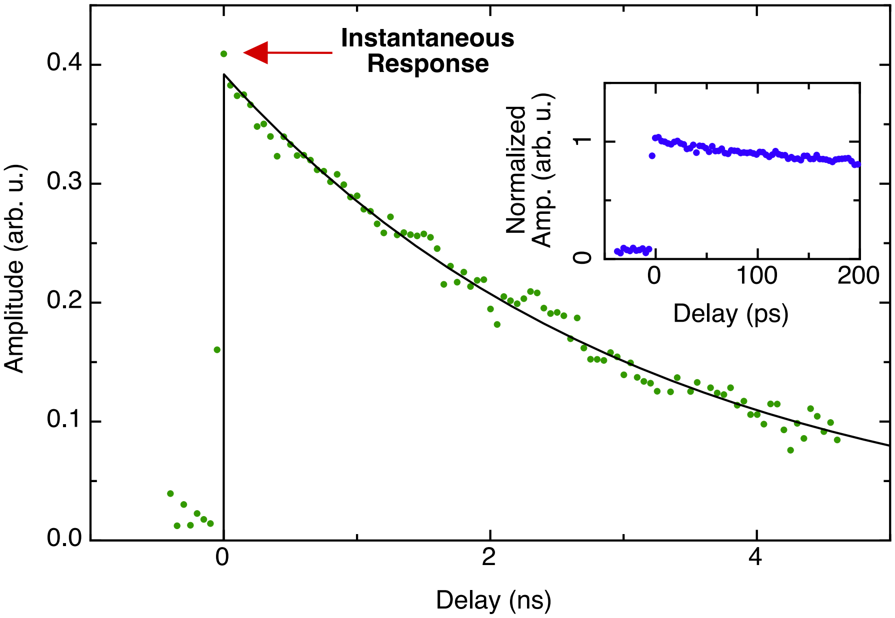

Figure 2.9: Example of the decay in Rhodamine 6G solution of an excited-state transient grating with a spacing 1.83 μm. The small peak at zero represents the instantaneous non-linear response. The solid line is a fit to an exponential decay. Inset: The first 200 ps showing immediate build-up and the initial decay in Rhodamine 6G.

α represents the mean coefficient of absorption, $L = d/\cos\theta$ is the interaction length determined by the thickness of the sample and the incident angle, λ is the wavelength of the probe beam, and Δn and $\Delta\alpha$ are the modulated amplitudes of the refractive index and of the absorption coefficient, respectively.

The formulation above assumes a uniform absorption component. In the case where the grating is written by beams that are absorbed, and therefore has a depth profile, Eqn. 2.16 is no longer accurate. The attenuation of the pump beams must then be taken into account with an attenuation factor A_α described as [13]

$$A_\alpha = \frac{1 - e^{-\alpha L}}{\alpha L} e^{-\alpha L/2}, \tag{2.18}$$

where α continues to represent absorption coefficient, and L is the sample thickness. In the limit of small diffraction efficiency, the diffraction efficiency can be expressed

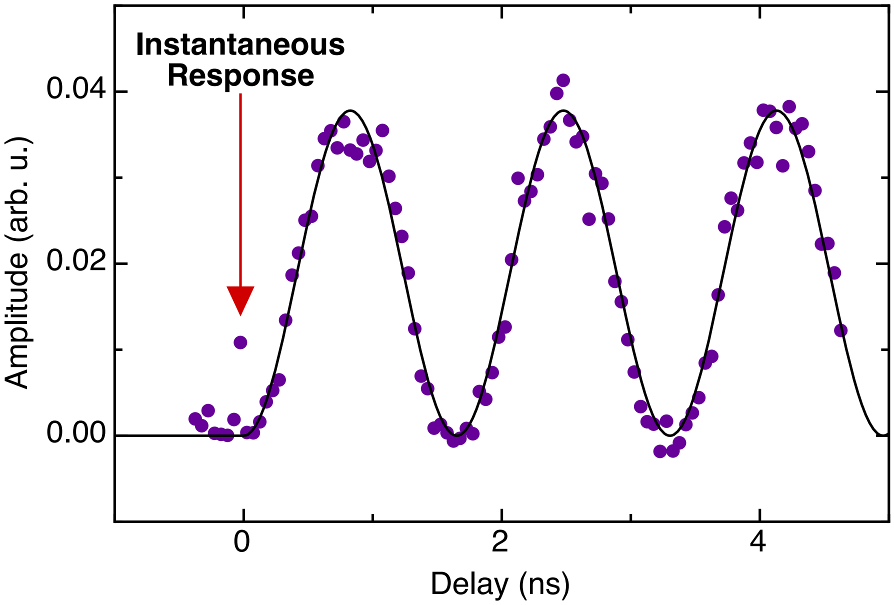

Figure 2.10: Example of oscillations in the signal of an organic molecule in solution from laser induced acoustic waves caused by a density grating of spacing 1.83 μm. Note the small peak at zero representing the instantaneous non-linear response. The solid line is a fit to Eqn. 2.21

as

$$\eta = [A(t)LA_\alpha]^2 . \tag{2.19}$$

A typical decay of the excited state that causes the transient grating can be seen in Fig. 2.9. The sample used here is a dye solution of Rhodamine 6G, and shows a standard exponential decay.

Not all excitations will decay exponentially. Chapter 4 will detail the quadratic recombination shown when bimolecular interactions occur.

2.4.3 Acoustic Waves

The optical generation of ultrasonic waves inside a sample is another observable in transient grating pump & probe experiments. The acoustic waves appear as oscillations in the data, as seen in Fig. 2.10.

The acoustic grating is built by changes in the optical properties of the crystal caused by local changes in density. The local changes in density are induced by a fast discharge of heat from molecules that have been promoted to an excited state or electrostrictive coupling of the electromagnetic and acoustic fields. [14, 15] In samples with very large absorption, thermally induced gratings are predominant, making the electorstrictive effect negligible.

The induced acoustic wavelength λ_S in the sample corresponds to the spatial modulation of the interference pattern that creates the grating,

$$\lambda_S = \frac{\lambda}{2\sin(\theta)} \tag{2.20}$$

where λ is the wavelength of the excitation pulses and θ is the half angle between the beams producing the interference pattern. Eqn. 2.20 is exactly the same as Eqn. 2.3 used to determine the grating spacing. The acoustic response that occurs along the grating wavevector in the sample can be represented as [15]

$$S_{22} = A_S(\cos ky - \frac{1}{2}[\cos(\omega t + ky) + \cos(\omega t - ky)] = A_S \cos ky(1 - \cos \omega t), \tag{2.21}$$

where A_S is the amplitude of the oscillation and S_{22} is the strain component defined by

$$S_{22} = \frac{\partial u_2}{\partial y}. \tag{2.22}$$

with u_2 representing displacement along the y-direction.

The grating spacing may be altered by a change in crossing angle or excitation wavelength. By using the grating spacing and the period of the oscillations ($T = \frac{2\pi}{\omega}$), the speed of sound inside the material may be determined by the ratio of the two quantities, $v_{sound} = \frac{T}{\Lambda}$.

2.5 Raman Nath vs Bragg Diffraction

When investigating diffraction gratings, there are two regimes that are commonly treated: Raman-Nath and Bragg diffraction [16, 17]. Raman-Nath diffraction is typically associated with a thin grating that produces several diffracted waves. Bragg diffraction is associated with thicker gratings that only produce one wave when the Bragg condition is satisfied.

Various criteria have been presented in the literature to determine the regime in which a phase grating is operating. One such criterion was proposed by Klein and Cook [18] where the parameter Q is used to determine whether a grating is "thick" or "thin", with Q expressed as

$$Q = \frac{2\pi\lambda_0 L}{\Lambda^2 n_0}. \tag{2.23}$$

Here L is the grating thickness (as determined by the absorption length and thickness of the crystal), λ_0 is the wavelength of the excitation light, Λ is the grating spacing (as determined by the wavelength and the crossing angle of the excitation pulses) and n_0 is the mean refractive index. When Q values are less than one, a thin grating is assumed and the Raman-Nath diffraction is present. For very large Q values (greater than 10) a thick grating is assumed to be responsible for Bragg diffraction.

Moharam et. al. [16, 17] proposed an alternative criterion that does not depend explicitly on the thickness of the grating. Their proposed parameter, ρ, is defined as

$$\rho = \frac{\lambda_0^2}{\Lambda^2 n_0 n_1}. \tag{2.24}$$

using the same nomenclature as was used in the Q parameter, with the addition of n_1 representing the modulation of the refractive index. ρ values less than one result in diffraction from a Raman-Nath regime, while ρ values significantly larger than one indicate the Bragg regime is responsible for diffraction.

The freedom to alter the crossing angle in the phase conjugate set-up allows for experiments in both the Bragg and Raman-Nath regime, while the very small, fixed crossing angle in the forward facing set-up keeps those experiments in the Raman-Nath regime for all wavelengths when using thin samples (~ 10 μm in thickness). Although the Raman-Nath grating produces additional diffracted waves resulting from the non-phase matched conditions for the three input pulses, the phase matched wave is the only one that was monitored. See Appendix A for all Q and ρ values used in this work.

2.6 Benefit of Transient Grating Experiments

The benefits of this transient grating pump & probe experiment over other pump & probe methods are profound. In most pump & probe experiments, the transmission of the probe beam is monitored for photoinduced changes in absorption. Transient grating experiments are also sensitive to photoinduced changes in the refractive index, and monitor a distinct, backgroundless signal pulse, not the probe pulse. As such, they have a higher sensitivity than conventional methods.

To repeat in other words, the benefits of using transient gratings as an experimental method to detect excitations in the material are two fold. First, the use of a transient grating results in a background free signal. The signal is created via Bragg diffraction; if the transient grating is not present, there is no signal. This is advantageous compared to other methods of pump and probe spectroscopy, where the transmission of a probe beam is monitored. Because transient gratings are backgroundless, the method is therefore sensitive to even slight modifications in refractive index or absorption

In addition, variation of the grating spacing can allow the differentiation between relaxation phenomena that are caused by local effects and relaxation that is caused by a washing out of the grating due to transport [19, 20].

Chapter 3

Introduction to Molecular Crystals

The transport of energy via excitons in molecular materials is a fundamental physical process that has several interesting and peculiar properties. Excitons in these materials are localized states and have large binding energies. The large binding energy means that dissociation of excitons into free electrons and free holes occurs mostly via interaction with defects and interfaces.

Molecular materials are attractive for applications because they can be engineered to efficiently absorb photon energy. However, their use for solar energy harvesting will always depend on exciton diffusion towards an interface as one key energy transport process. In fact, state-of-the-art organic photovoltaic cells require bulk heterojunctions [21] that minimize the required exciton diffusion length. This is due to weak exciton diffusion in most polymeric materials, with diffusion lengths confined to less than 50 nm.

Although the first experiments on molecular crystals such as anthracene and their excited states date to shortly after the invention of the laser [22, 23], the processes that govern the dynamics of excitons in these crystals have not been fully characterized and understood. This chapter discusses excitons in molecular crystals, describes the molecular and crystal structure of the rubrene single crystal and the physical mechanisms of exciton dynamics in the crystal, and reviews what makes rubrene a material worthy of further investigation, while providing a brief analysis of recent research.

3.1 Excitons in Molecular Material

Certain types of molecular crystals are bound by van der Waals forces (as opposed to covalent or ionic forces), and show small overlap between molecular orbitals. This class of materials also has small band-widths, resulting in small mobility. Excitons are dominant at room temperature in these materials, and are easily created by the absorption of a photon, but they are difficult to dissociate into free carriers.

A common example of molecular crystals are those composed of hydrocarbons, such as the polyacenes. Some organic crystals have possible fields of application that are similar to those of inorganic semiconductor, and are occasionally referred to as organic semiconductors.

Excitons in the polyacene organic crystals have high binding energies with wavefunctions that are essentially localized to a molecular site [24]. Excitons in most inorganic crystals, like silicon, are delocalized and their binding energies are that of a loosely bound electron-hole pair, and are comparable to the thermal energy.

There are two possible neutral excited spin states in which a molecule with two electrons outside closed shells can exist. Consider the two electrons each having two possible spin orientations. There are then a total of four possible spin states for the system, and therefore only four possible spin eigenfunctions, one antisymmetric and three symmetric. The antisymmetric spin eigenfunction has total spin angular momentum of zero, and is called the singlet state. The three symmetric spin eigenfunctions have total spin angular momentum of 1, and are called the triplet states. [25]

The Pauli exclusion principle requires the ground state of a molecule to have two electrons in a singlet state in the highest occupied molecular orbital. When the molecule is excited by absorption of a photon, one electron is promoted to an excited singlet state ($S_0 \to S_n$) while maintaining spin orientation, which conserves the spin angular momentum.

If the only interaction between the two electrons is the electrostatic Coulomb repulsion, then the antisymmetric singlet state will be at a higher energy than the symmetric triplet states. The triplet state is at a lower energy than the singlet due to exchange symmetry, which increases the expectation value of the distance between the two electrons in the triplet causing the Coulomb energy to be smaller. [26]

3.1.1 Singlet Fission and Triplet Fusion

Because triplet excitons can have an energy significantly lower than that of the singlet exciton, photoexcited singlet states in organic molecular crystals can transition via an interaction with a ground state molecule into two triplet states with a total spin of zero, in addition to radiative or nonradiative decay back to the ground state. The former can be seen as a first step in a fission process that can lead to the two triplet excitons independently diffusing in the crystal, a process that could play a key role in organic photovoltaics [27].

In a simplified system of two interacting molecules with four electrons total, the singlet exciton can spontaneously split via a spin-allowed fission process into two triplets that, combined, have overall singlet characteristics. This requires that there be at least two molecules close to each other to accommodate the fission process, making singlet fission a property of the molecular assembly. The fission process also requires that the energy of the excited singlet state be at least twice the energy of the triplet state [28].

A simplified fission process has been demonstrated in a system of two covalently connected molecules of tetracene by Müller *et. al.* [29]. In a crystal, we may analogously consider two neighboring molecules in the crystal lattice participating in the fission process. Fig. 3.1 shows a schematic progression of events.

Note that fission may not immediately lead to two independent triplet states, but instead to a quantum superposition of two triplets with one singlet.

$$S_1 \Leftrightarrow (T_1 + T_1) \Leftrightarrow T_1 + T_1 \tag{3.1}$$

This superposition has been identified, for example, by the telltale quantum beats in the prompt and delayed fluorescence of the tetracene crystal [30, 31]. Either component of the superposition may decay into a new state; the singlet could radiatively or non-radiatively recombine to the ground state, or one of the triplets could

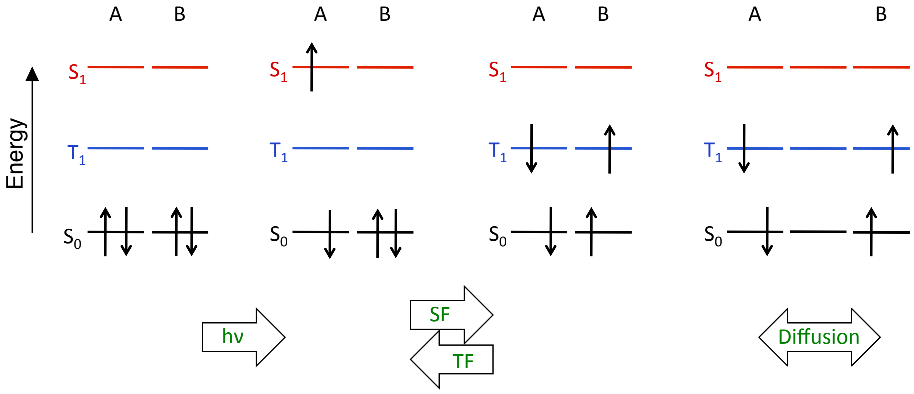

Figure 3.1: Schematic of the creation of triplets by singlet fission (SF). The absorption of light creates a singlet exciton. The transfer of energy via fission to a neighboring molecule creates two triplet excitons. The transfer of energy back to the original molecule via triplet fusion (TF) recreates the singlet. The triplets may diffuse away only once the quantum superposition decays.

diffuse away from the other. This is seen in the last step of Fig. 3.1, as the quantum superposition first decays into two independent triplets, and then those two triplets diffuse independently from each other. Thus, the quantum superposition can decay via two main processes: recombination of the singlet state or separation of the triplet pair.

Once the quantum superposition has decayed, a diffusing triplet exciton can meet another triplet exciton with the correct spin and undergo fusion to create a spin zero singlet again. Alternatively, the triplet can dissociate at a defect or surface boundary, or can relax in other ways. Dissociation is desirable for photo-voltaic applications because it is how charge would be harvested from the sample. The triplet state ends up being responsible for many of the remarkable characteristics of molecular crystals.

3.2 Rubrene

Rubrene (tetraphenylnapthacene, $C_{42}H_{28}$) is a material of great interest for study, not only to investigate the fundamental physics that govern its characteristics, but also to function as a model for a class of molecular materials that have potential for being developed for use in optoelectronic devices. Studying exciton dynamics in rubrene will provide fundamental knowledge that may one day be applied to crystalline organic photovoltaic cells with a controlled large diffusion length, which could even lead to the possibility of eliminating the need for bulk heterojunctions.

Although rubrene has recently been the subject of a great amount of study, there is still much to to be determined regarding the exciton dynamics in this crystal. As one example, various pump and probe time dynamics experiments have yielded partially contradictory results on the singlet exciton lifetime. This has lead to various inconsistent models of singlet exciton relaxation after photoexcitation. It is at present not clear what the lifetime of the initially photoexcited singlet state is, or how fission into triplet states should be interpreted. Experimental results recently published by Tao et al. [32] and Ma et al. [33] are either conflicting, or the interpretation of the data is attributed to wildly differing physical phenomena.

Investigating exciton dynamics in rubrene is particularly promising because of a set of unique properties of this crystal, namely a relatively large hole mobility [8, 34–36], large triplet diffusion length of 4 μm [37], long triplet lifetime of 100 μs [38, 39], large singlet fission and triplet fusion probabilities [38, 40], and large delayed photocurrent [41, 42] due to triplet dissociation.

3.2.1 Crystal Structure

A member of the polyacene family, rubrene is a polycyclic aromatic hydrocarbon comprised of a chain of four benzene rings and four phenyl groups attached to the center rings. The four benzene rings are structurally equivalent to the tetracene molecule. The single crystals are centrosymmetric with an orthorhombic crystal structure (lattice parameters of a = 14.4 Å, b = 7.18 Å, and c = 26.9 Å, where we define the crystallographic axes in the same way as Refs. [8, 34, 35, 37, 43]). There are four molecules per unit cell. Fig. 3.2 shows the molecular and crystalline structure for both rubrene and tetracene.

Although the molecular structures are similar, the crystal structures of rubrene

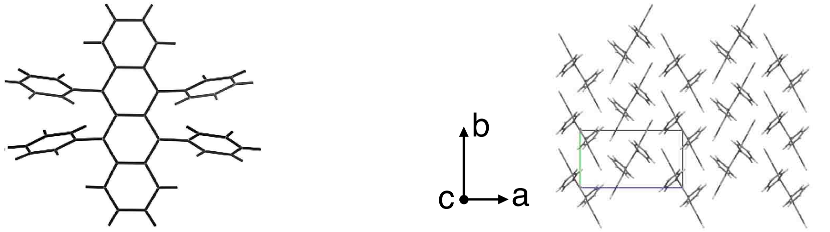

Rubrene Molecule **Rubrene Crystal Structure**

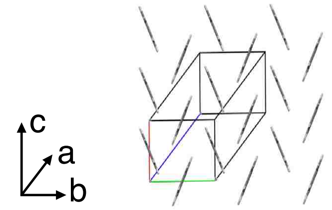

Tetracene Molecule **Tetracene Crystal Structure**

Figure 3.2: Molecular structure for rubrene and tetracene, and crystalline structure in the *ab* plane for rubrene and tetracene.

and tetracene are quite different. The different arrangement of molecules in the crystals lead to widely different physical properties. While both have a herringbone structure along the *b*-axis, the molecules in tetracene crystals have all their long axes parallel to each other, whereas in rubrene it is the short axes that are parallel.

This is important because the transition dipole moment is along the short axis of the molecule for all polyacenes [44]. As Fig. 3.2 shows, the molecules in crystalline tretracene are then oriented with transition dipole moments parallel to the *ab*-plane, which is normally the orientation of the largest facet of as-grown tetracene crystals, and the orientation of the transition dipole moments follows a herringbone structure in the *ab*-plane. As a consequence, the absorption experienced by a beam of light propagating perpendicular to the largest facet of naturally grown tetracene crystals experiences large absorption, weakly dependent on the light's polarization direction. In the rubrene crystal, on the other hand, all molecules have their transition dipole moment parallel to each other, along the c-axis of the crystal, which is normally perpendicular to the large facet of as-grown crystals. As a consequence, the strong

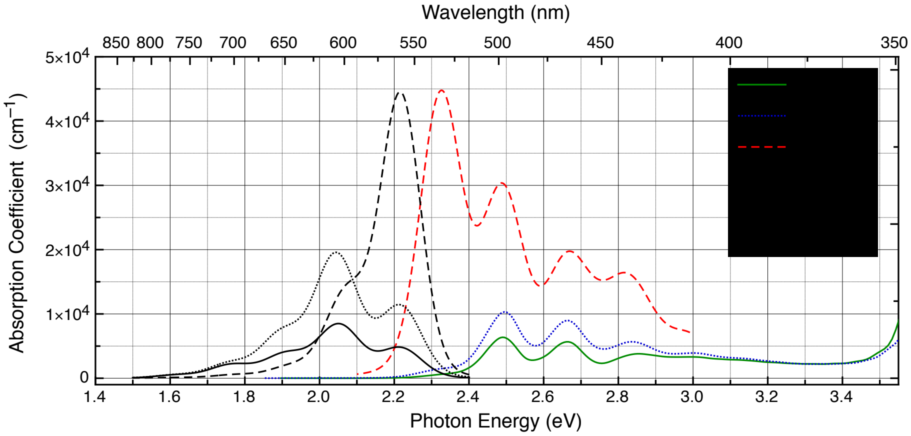

Figure 3.3: Intrinsic absorption spectra and photoluminescence spectra of pristine rubrene single crystal samples [43]. The 0.10 eV Stokes Shift is due to low frequency molecular deformations. The spectra show typical vibronic progression with distances between absorption and emission peaks of 0.17 eV and 0.15 eV, respectively [43].

absorption of the rubrene molecules is usually inaccessible to light propagating perpendicular to the surface of as-grown crystals. In addition, the parallel orientation of all molecular transition dipole moments in the c-direction causes light absorption and luminescence emission in rubrene crystals to be extremely anisotropic [43].

The crystalline *b*-axis of rubrene has good π-orbital overlap [45]. This is thought to be responsible for the relatively high hole mobility, with measured values of hole mobility in rubrene single crystals ranging from approximately 10 cm^2/Vs [46] to 42 cm^2/Vs [47] along the *b*-axis, while crystalline tetracene has a measured mobility significantly smaller than the range of rubrene, being only 1.6 cm^2/Vs [48].

3.2.2 Spectral Properties: Absorption and Photoluminescence

Fig. 3.3 shows the intrinsic absorption and photoluminescence (PL) spectra of pristine rubrene for the spectral ranges used in this study.

The absorption spectrum for *c*-polarized light has a strong absorption peak centered at 2.32 eV followed by several smaller peaks, 0.17 eV apart [43]. This is a typical vibronic progression that is also seen in the corresponding PL spectrum, characterized by a first peak near 2.22 eV followed by bands spaced 0.147 eV apart [43]. The distance between vibronic peaks is on the order of the stretching frequency of carbon bonds, and both the strongest c-polarized absorption peak and the strongest c-polarized emission peak correspond to a transition between the ground states of this high frequency vibrational modes, with the Stokes shift of 0.1 eV corresponding to the effect of lower frequency molecular deformations.

Rubrene has an anisotropic index of refraction($n_a \approx 1.7, n_b \approx 1.9$ and $n_c \approx 2.0$ along the $a-$, $b-$, and $c-$axes, respectively. [49, 50]) and anisotropic absorption coefficients [37]. For light with components of its electric field along the b- and c-axis, the following equation can be used as an approximation valid for calculating the effective absorption coefficient when the birefringence is small

$$\alpha(\theta) = \alpha_{a,b} \cos^2 \theta + \alpha_c \sin^2 \theta. \tag{3.2}$$

Here θ is the angle of incidence, and α_i is the absorption coefficient along the ith axis.

The PL spectrum of rubrene also indicates whether the samples being investigated are pristine or non-pristine. The spectrum has been shown to have an altered shape in certain kinds of rubrene crystals. The altered spectrum peaks around 650 nm instead of having its normal peak emission at 564 nm for c-polarized and 610 nm for ab-polarized emission in pristine samples [43].

3.2.3 Singlet Fission in Rubrene

The rubrene single crystal has triplet excitons with approximately half the energy of its singlet excitons, allowing a photoexcited singlet exciton to split its energy and transition to a pair of neighboring molecules that are both in a triplet state with a total spin zero. This process is called “fission.” Rubrene is, in fact, characterized by a particularly efficient fission mechanism that leads to a large majority of photoexcited singlet states ($\sim$ 95%) ultimately transforming into triplet excitons [38–40]. Triplet fusion, where the energy of the triplet pair is pooled such that they transition back to an excited and ground state singlet pair, is also very efficient in rubrene. There are few molecular assemblies suitable for efficient singlet fission *and* triplet fusion [51], making rubrene an excellent test system for fundamental studies targeted at understanding the fission and fusion processes.

Previous pump and probe experiments in rubrene showed that triplets appear within ∼10 ps [33, 52]. PL from singlets decreases over a few nanoseconds before settling into the power-law dominated triplet fusion process responsible for the delayed PL. Triplets have relatively long lifetimes of about 100 μs [38], which contribute to their long diffusion length of 4 μm in the b-axis direction [37]. Since the triplet's life time is much longer than the singlet's, the fusion process can continue for longer than the singlet radiative lifetime. The triplet state is a dark state, so any detection of PL after the singlet lifetime must come from singlets that have been produced by triplet fusion. We can therefore track triplet diffusion by singlet PL [37]. Detecting the delayed PL indicates that there is very efficient fission/fusion occurring in rubrene. The dynamics of singlet fission and triplet fusion can be described by the time evolution of the singlet and triplet densities [38].

Triplet excitons can also be created via nonradiative intersystem crossing [53], but intersystem crossing probabilities in rubrene are so low, and singlet fission is so efficient, that the majority of triplets are created via singlet fission.

Singlet fission in rubrene single crystals has not yet been consistently described. Tao *et al.* [46] have observed an ∼ 100 ps fast decay of a photoinduced infrared absorption band which they assigned to singlet excitons, but they interpreted the decay as caused by exciton dissociation, not fission. Furube *et al.* [54] observed transient absorption kinetics in the near infrared which they interpreted as singlet exciton fission into triplets with a time constant of 10 ps. Ma *et al.* [33, 52] identified photoinduced absorption bands in the visible spectral region, which they assigned to singlet and triplet excitons, and they derived a ∼ 2 ps time for singlet fission from higher vibrational states and a ∼ 20 ps time for singlet fission from the lowest vibrational state. With the exception of Ref. [46], transient absorption measurements have been largely interpreted as a singlet-to-triplet fission process that occurs on a time scale ranging from from ∼ 2 ps to ∼ 20 ps, sometimes even in nominally amorphous films [33, 52, 54, 55]. However, Piland *et al.* [56] measured photoluminescence transients in rubrene films that they interpreted as indicative of a fission time of 2 ns. The inability to detect tell-tale quantum beats in the rubrene photoluminescence [31] led them to hypothesize an insufficient fission rate. In general, time resolved photoluminesence measurements have not shown a clear transition from an initial singlet luminescence transient on the picosecond time scale (matching the singlet lifetime) to the typical power-law decay expected for a dense triplet population [24, 38, 39, 57, 58]. On the contrary, photoluminescence transients have shown a multiexponential decay with time-constants ranging from 80 ps to a few nanoseconds [33, 39, 55].

It is worth noting that in general a singlet exciton transitions into a quantum superposition of the singlet state with two triplet states having a total spin of zero [31]. This superposition state can then decay by radiative recombination of the singlet component, or it can decay into two triplet excitons that can diffuse independently. It is the latter possibility that is singlet exciton fission into two independent triplet excitons [28]. It follows that the $\sim$ 10 ps lifetime mentioned above can also be interpreted as the time needed to reach an equilibrium singlet-triplet superposition state, and not necessarily the time to create two independent triplet excitons, which could be much longer, similar to the nanosecond-scale decays observed in photoluminescence transients [56].

3.2.4 Delayed Photocurrent

An important hurdle to clear in terms of developing organic crystals for use in devices is the dissociation of excitons into free charge carriers. The large binding energies of triplet excitons, up to $\sim$1.5 eV [1], make this no small feat.

Najafov *et al.* saw a small instantaneous release of carriers in photocurrent experiments [42] that may be an effect of direct disassociation of some singlet excitons into free electrons and holes. A second, generally stronger component of the photocurrent is built up on the order of microseconds, indicating a delayed release of the charge carriers. This build-up time matches the triplet lifetime. If the build-up of the photocurrent (representing dissociated triplets) is compared with the square root of the PL (representing triplet density), there is a definite relationship where, as the current builds up, the PL decreases. This relationship indicates that the charge carriers responsible for the photocurrent originate from triplets.

Rubrene is an organic crystal with many interesting optoelectronic properties. The particularly efficient fission mechanism which results in 95% of photoexcited singlet states transforming into triplet excitons, the large triplet diffusion length of 4 μm and the long triplet life time of 100 μs represent just a few of these properties. These properties lead us to study excitons in the ordered, high quality rubrene single crystal. The results from these studies are presented in the next three chapters.

Chapter 4

Transient Grating Decay Dynamics

Photoexcited singlet states in organic molecular crystals can transition into two triplet states with a total spin of zero, in addition to radiatively or nonradiatively decaying back to the ground state. The former can be seen as a first step in a fission process that can lead to the two triplet excitons independently diffusing in the crystal, a process that could play a key role in organic photovoltaics [27]. As stated in Chapter 3, rubrene single crystals are characterized by a particularly efficient fission mechanism that leads to a large majority of photoexcited singlet states ultimately transforming into triplet excitons [38, 40].

Transient grating experiments allow us to observe time dynamics of an excited state by detecting the relaxation of a photoinduced transient grating. Once the crystal is excited by two pump beams, the presence of excitons changes the refractive index or absorption of the material which results in a diffraction grating inside the material. If the change in refractive index or absorption is large enough, the amplitude of the transient grating can be determined by diffraction of a probe beam.

The decay rate of the grating amplitude is highly sensitive to the photoexcitation density, and because of high triplet fusion probabilities in rubrene crystal this could be a possible explanation for the observed variability of photoluminescence decay times that have been reported in rubrene. In this chapter, we will monitor the decay of the photoinduced transient grating.

4.1 Experimental Details

In this chapter, we describe pump & probe transient grating experiments used to investigate excited-state dynamics on a time scale between 20 ps and 10 ns in vapor-transport grown rubrene crystals. We used the phase conjugate configuration to create the transient grating with an excitation and detection wavelength of 532 nm from the pulsed Ekspla Nd:Yag laser. This wavelength allowed excitation to the ground vibrational state of the singlet exciton [43], and falls at the long-wavelength edge of a transient absorption band that has been assigned to triplet absorption [33, 54, 59]. We used 20 ps laser pulses crossing at angles ranging from 4.8° to 90°. This created transient gratings with spatial periods between 6.3 μm and 0.4 μm, respectively. The transient grating was detected by measuring the diffraction efficiency of a time-delayed pulse incident at the Bragg angle via a photomultiplier tube (PMT). The output voltage of the PMT was integrated by a boxcar integrator over a 30 ns time-interval defined by the gate width, and then averaged over multiple repetitions to produce a clean, clear data set which was recorded by the computer.

All data shown in this work were obtained using a pristine rubrene sample, verified by measuring its photoluminescence spectra [43], with dimensions of ~ 1 mm along the a and b directions, and 12 μm along the c direction. This crystal was mounted with the c-axis along the bisectrix between the two excitation beams (see Fig. 4.1, inset), and the b-axis parallel to the grating wavevector. We chose the excitation light to be a-polarized, which gave the strongest signal because of the relatively long absorption length of ~ 15 μm at 532 nm [43], leading to a thicker grating and less attenuation of the counterpropagating probe pulse. We also used other samples, different orientations, and different polarizations, and in all cases the observed dynamics were the same as what we report below.

4.2 Determining the Nature of the Grating

The spatial dependence of the light intensity in the photoexcitation pattern is

$$I(y, z) = I_0[1 + m_0 \cos(k_g y)]e^{-\alpha_a z} \tag{4.1}$$

where y and z are the coordinates along the b and c axes of the crystal, respectively. α_a is the absorption coefficient for a-polarized light at 532 nm, and k_g is the modulus of the grating wavevector. $I_0 = I_1 + I_2$ is the sum of the intensities of the two interfering pulses, and m_0 is a modulation index given by $2\sqrt{I_1 I_2}/I_0$. Since a photoexcited molecule has, in general, a different polarizability than a ground-state molecule, photoexcitation can create both an absorption and a refractive index grating that are initially in-phase with the light-intensity pattern. Recall from Chapter 2 that the diffraction efficiency of a probe pulse incident at the Bragg angle is [12]

$$\eta(t) = \left| \sin\left(\frac{\pi L}{\lambda} A(t)\right) \right|^2, \tag{4.2}$$

where L is the effective interaction length, λ is the light wavelength, and $A(t)$ is the amplitude of the first Fourier component of the photoinduced grating. It is in general complex-valued, with an imaginary part related to absorption modulation and a real part $\mathrm{Re}[A(t)] = \Delta n$ given by the refractive index modulation [12]. Immediately after photoexcitation and in the absence of saturation effects, $A(0) \propto I_0 m_0$ and the grating is purely sinusoidal.

Figure 4.1 shows the time-dependence of the diffraction from the photoinduced grating for varied excitation densities. The grating amplitude grows immediately during the length of the excitation pulses, and then relaxes within a few nanoseconds. The data also clearly show a high frequency oscillatory component riding on top of the slower nanosecond decay.

The frequency of the oscillations depends on the grating spacing, as is shown by Fig. 4.2. This means that the oscillations in diffraction efficiency are caused by laser-induced ultrasonic waves [60, 61]. The grating amplitude in Eq. (4.2) can then be written as

$$A(t) = A_{exc}(t) + \frac{A_s}{2}(1 + \cos\omega_s t), \tag{4.3}$$

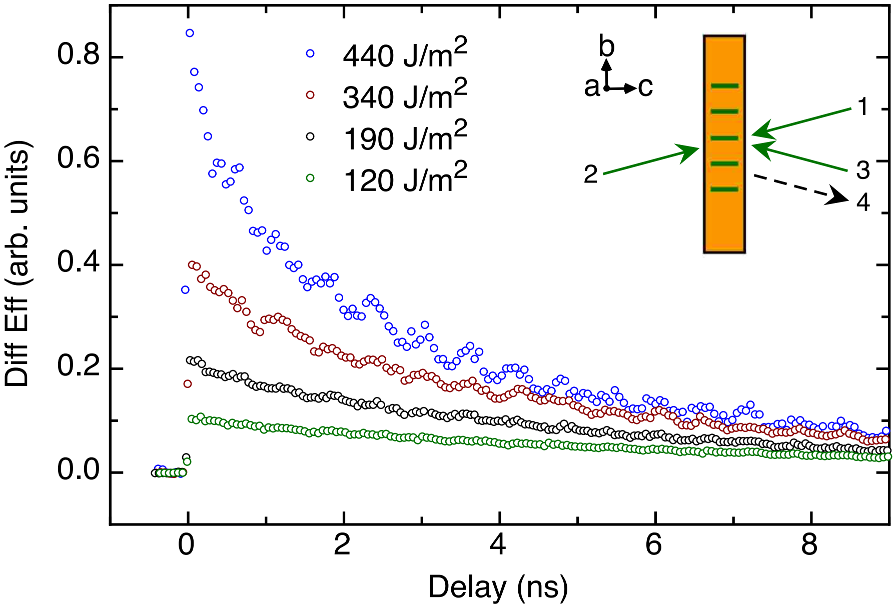

Figure 4.1: Time-dependence of the transient grating amplitude after impulsive excitation in rubrene at a grating spacing of 1.4 μm. Data sets were taken with total absorbed fluences of 120, 190, 340, and 440 J/m^2, correspond to excitation densities of 2, 3, 6 and 8 $\times$ 10^{19} photons/cm^3, respectively. Inset: Grating formed for the phase conjugate orientation.

where $A_{exc}(t)$ is the amplitude of the background excited state modulation, A_s is the amplitude of the ultrasound grating, and $\omega_s = v_s k_g$ is the angular frequency of the ultrasound wave with speed v_s. The solid curves in Fig. 4.2 are least squares fits to the data using this expression with an appropriate choice for the time-dependence of $A_{exc}(t)$ that we will discuss below. The acoustic speed extracted from fits at different grating spacings (see Fig. 4.3) is $v_s = 2.6 \times 10^3$ m/s, similar to results obtained in other organic crystals [60]. In addition, we find that a good fit of the experimental data is only possible using real-valued $A_{exc}(t) > 0$ and $A_s < 0$ so that the oscillation caused by the acoustic wave reduces the the diffraction that would be caused by the background grating alone. The data cannot be fitted well if one assumes that $A_{exc}(t)$ has a large imaginary part as would be caused by an absorption grating, and it can also not be reproduced well when assuming that the ultrasound grating is caused by electrostriction [60, 61].

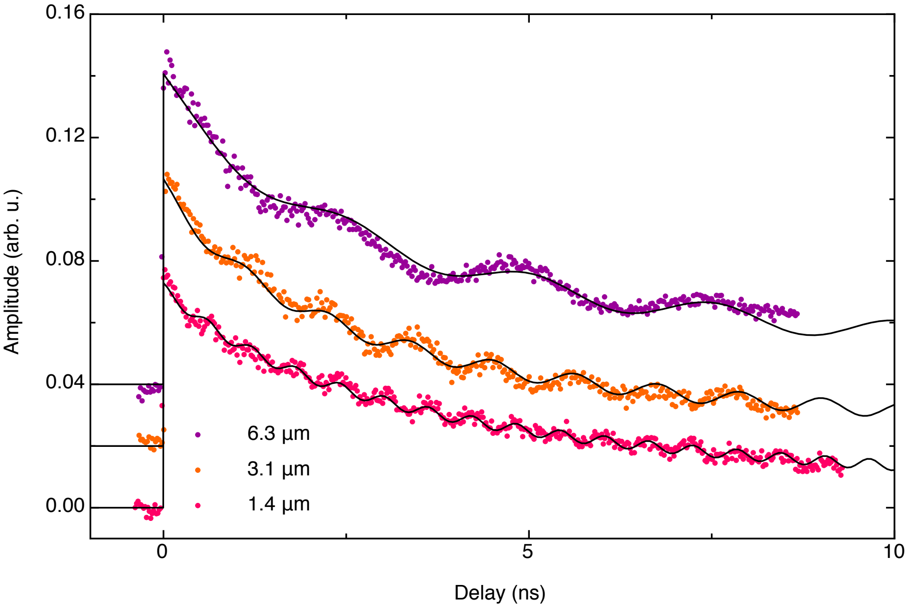

Figure 4.2: Grating spacing dependence of the acoustic wave frequency, offset to show detail.

From the fact that our data can only be modeled by Eq. 4.3 with real-valued amplitudes, and the fact that the ultrasound grating is a refractive index modulation, one must conclude that the grating that produces the nanosecond decay in our experiment is also a refractive index grating. The onset of the ultrasound oscillation corresponds to a dilation of the material in the higher intensity regions of the interference pattern. The amplitude of the longer-lived excitation grating must then be a positive index-change that is periodically reduced by the refractive-index decrease caused by elastic dilation, with the time-dynamics of the background grating obtained by connecting the maxima of the oscillation. We thus reach the important conclusion that the nature of the main signal that we are detecting is not an absorption modulation, but a refractive index modulation, likely caused by a higher polarizability of the excited-state molecules when compared to the undisturbed crystal. From the measured diffraction efficiency and Eq. 4.2 we estimate the refractive index change induced at an excitation density of 8×10^{19} photons cm^{-3} to be on the order of 0.008.

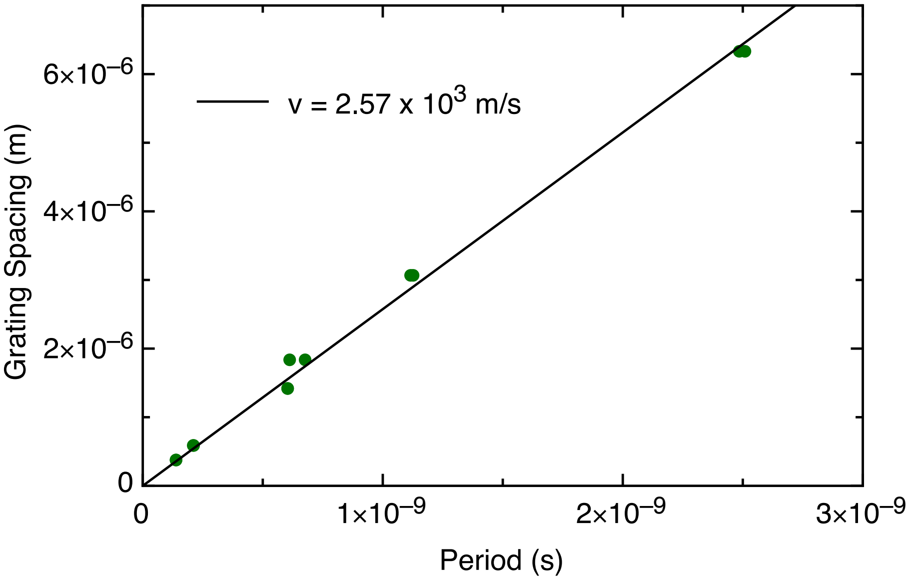

Figure 4.3: The grating spacing vs oscillation period for light polarized along the *a*-axis. The linear fit line indicates a consistent wave speed of 2.6×10^3m/s along the *a*-axis.

4.3 Determining the Nature of the Decay

Fig. 4.1 shows that the diffraction efficiency from the photoexcitation grating decays in a few nanoseconds, and that this decay is faster at higher excitation densities. The nanosecond decay is not a single exponential. Curve fitting with multiple exponentials would be possible, but with no clear distinction of decay time-constants. Instead, the fact that the decay becomes faster at higher excitation densities could be an indication that it is caused by the interaction of excited states created close to one another. To test this hypothesis, we first derive the time-dependence of the grating amplitude when its decay is caused by a bimolecular interaction process.

The spatial dependence of the first Fourier component of the photoinduced grating must have the same form as (4.1),

$$\rho(t, y) = \tilde{\rho}(t)[1 + m(t)\cos(k_g y)], \tag{4.4}$$

where $\tilde{\rho}(t)$ is the initial average density of (as yet unspecified) excited states in the crystal, which may be a function of depth, $m(0) = m_0$, and we do not explicitly write the slow decrease in the z-direction. Local quadratic recombination as described by $d\rho(t,y)/dt = -\gamma\rho(t,y)^2$ implies

$$\rho(t,y) = \frac{\rho(0,y)}{1+\rho(0,y)\gamma t}, \tag{4.5}$$

where γ is a bimolecular interaction rate. Developing this into a Fourier series and casting its first two terms in the form (4.4) gives

$$\begin{aligned} \tilde{\rho}(t) &= \frac{1}{\gamma t}\left(1-\frac{1}{C}\right) & (4.6)\\ m(t) &= \frac{2}{m_0}\left(\frac{1}{C-1}-\frac{1}{\rho_0\gamma t}\right), & (4.7) \end{aligned}$$

where $\rho_0 = \tilde{\rho}(0)$ and

$$C = \sqrt{1+\rho_0\gamma t[2+\rho_0\gamma t(1-m_0^2)]}. \tag{4.8}$$

This result is valid for any initial modulation m_0 of the grating, but it is useful to consider the limit of a small modulation index, $m_0 \to 0$. In this limit one finds

$$\begin{aligned} \tilde{\rho}(t) &= \frac{\rho_0}{1+\rho_0\gamma t} & (4.9)\\ m(t) &= \frac{m_0}{1+\rho_0\gamma t}. & (4.10) \end{aligned}$$

The diffraction from the photoinduced grating as described by Eq. 4.2 is governed by the amplitude $A(t) \propto \tilde{\rho}(t)m(t)$. The effect of quadratic recombination is seen both on the average density, $\tilde{\rho}(t)$, as well as on the modulation index, $m(t)$. As a consequence, $A(t)$ follows a power law with an exponent of 2 instead of the simple decay with an exponent of 1 that appears in Eq. (4.5). This time-dependence will dominate over the effects of quadratic recombination on a possible inhomogeneous profile of the grating in the direction perpendicular to the crystal's surface.

To assess if the time-dynamics shown in Fig. 4.1 are indeed caused by a quadratic recombination process, we measured the grating decay over a wider range of excitation pulse fluences and, following Eq. (4.2), derived the time-dependence of the grating amplitude $A(t)$ by taking the square-root of the diffraction efficiency. The

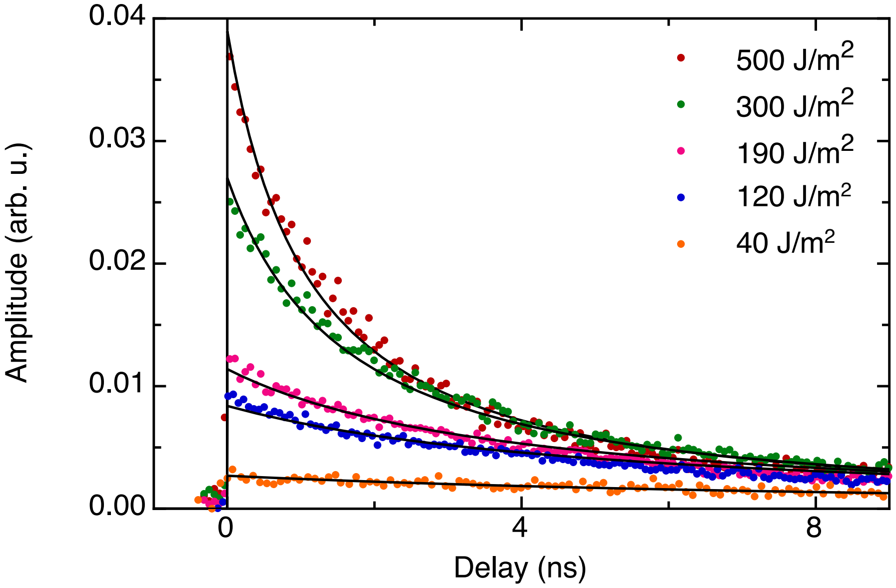

Figure 4.4: Photoinduced grating dynamics at different excitation densities at a grating spacing of 0.6 μm. Total absorbed fluence at the surface of the crystal ranges between 40 and 500 J/m^2.

results are shown in Fig. 4.4. We then performed a simultaneous least squares fit of the resulting data using $A(t) = B\tilde{\rho}(t)m(t)$ and Eqs. (4.6-4.7). Here, the only fitting parameters were the proportionality constant B (same for all data sets) and the product $\gamma\rho_0$ for each of the different excitation densities. We stress that in this way the time-dependence of each data set is fit with *only one fit parameter*, essentially the initial average density ρ_0. The results are plotted in Fig. 4.4 and they show a very good agreement between data and model, clearly showing that the strength of the diffracted signal at time $t = 0$ correlates with the grating decay rate in exactly the way predicted by a quadratic recombination model.

Figure 4.5 shows how the product $\rho_0\gamma$ obtained for different data sets relates to the actual average excitation density used in the corresponding experiment, which was calculated from

$$\rho_0^{exp.} = n_a t^2 \alpha_a \frac{\lambda}{hc} F_{tot}, \tag{4.11}$$

where F_{tot} is the the sum of the fluences of the two excitation pulses as obtained from pulse energies and the beam waist at the surface of the crystal, n_a is the index

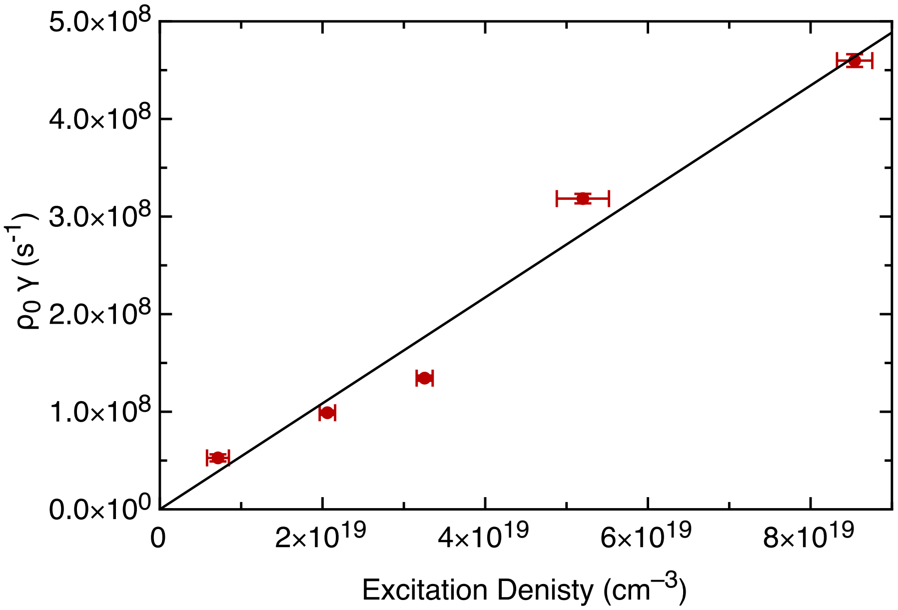

Figure 4.5: The corresponding excitation densities for Fig. 4.4, correlating them to $\rho_0\gamma$, the one fitting parameter used to obtain the solid curves. A linear fit gives a value for the bimolecular interaction constant of $\gamma = (5.4 \pm 1.0) \times 10^{-12}$ cm^{3}s^{-1}.

of refraction along the a axis, t is the Fresnel amplitude transmission coefficient calculated from the incidence angle, and α_0 is the absorption coefficient at 532 nm [43]. The linear correlation displayed in Fig. 4.5 implies $\gamma = (5.4 \pm 1.0) \times 10^{-12}$ cm^{3}s^{-1}. This value is determined only by the observed decay dynamics and measured pulse fluences and it agrees well with previous estimates [38, 40]. Put another way, the measurements in Fig. 4.4 imply that quadratic recombination leads to the destruction of 50% of the original excitation after $\sim$ 3 ns at an average excitation density at the surface of the crystal corresponding to $\rho_0 \sim 0.5 \times 10^{20}$ cm^{-3}. Such an excitation density corresponds to an average distance between photoexcited molecules of only $\sim$ 3 nm. It is therefore not astonishing that interaction between excited states is possible at such small distances.

In addition to the data in Fig. 4.4, we also performed several experiments at other grating spacings, and in all cases we observed a behavior compatible with the one described above. Only at the shortest grating spacings, on the order of 0.4

μm obtained at 90° crossing angles, was an acceleration of the decay noted. While this could imply that, in addition to quadratic recombination, transport may be responsible for washing out the grating as excitons migrate from grating peaks to nulls, the experiment at these short grating spacings was difficult, with a low signal-to-noise ratio, and this possible contribution of transport could not be investigated further.

4.4 Determining the Nature of the Excited States

We finally come to a discussion of the nature of the excited states that we are detecting in the present experiment. Given the fact that photoexcited singlet states are expected to transform into two entangled triplet-state molecules within our pulse length, an obvious candidate for the excited states that we detect are triplet states. Ma *et al.* [33] identified a photoinduced absorption band peaking near 510 nm that they associated triplet excitons formed from singlet-to-triplet fission within 20 ps from photoexcitation. The refractive index change detected in our experiment, performed at 532 nm, could be associated both with this triplet exciton absorption, as well as with the absorption band assigned to singlet excitons in the same publication [33]. In the next chapter, we will discuss experiments performed with 1 ps laser pulses where we observed that the build-up of the signal reaches a quasi steady-state value in less than 10 ps, which compares well with the observations in Ref. [33], and implies that the index change we observe originates from triplets.

It is also possible to estimate the average distance traveled by free independent triplet excitons with the observed diffusion length [37] and lifetime [38] of 4 μm and 100 μs, respectively, to obtain a diffusion distance during a time of 3 ns of $(4\ \mu\text{m}) \times \sqrt{(3\text{ns})/(100\mu\text{s})} \approx 20$ nm. This estimate shows that it is at least conceivable that what we have observed on the nanosecond time scale is caused by the same triplet diffusion that is observed in steady-state. However this estimate does not properly take into account the quasi-one-dimensional diffusion and there is a relatively large latitude for different interpretations. As an example the triplet states observed in the present experiment could well still be in a coherent quantum superposition with a singlet state.

4.5 Discussion of Results

In this chapter, we demonstrated an alternative method for observing exciton dynamics in rubrene with a high sensitivity and a high time-resolution. The experiments have shown a power law decay that is indicative of a bimolecular interaction of excited states with a triplet component in rubrene over a time scale of nanoseconds and a distance of ~ 3 nm, corresponding to excitation densities on the order of $\sim 0.5 \times 10^{20}$ cm^{-3}. An important observation is that the decay rate is highly sensitive to the photoexcitation density, and because of high triplet fusion probabilities in rubrene crystal this could be a possible explanation for the observed variability of photoluminescence decay times that have been reported in rubrene.

Chapter 5

Transient Grating Build-Up Dynamics

Recall from Chapter 3 that excited singlets in rubrene are efficient at undergoing fission. Triplet excitons should be formed after photexcitation, as singlets undergo fission, with the fission rate determining the formation time of the triplet excitons. It is generally believed that the singlet-to-triplet fission process takes from $\sim 2\,\text{ps}$ to $\sim 20\,\text{ps}$ [33, 52, 54, 55]. We intend to verify what species of exciton we are detecting by remaining at the established excitation and detection wavelength of 532 nm and using a laser source with a 1 ps pulse width in order to complete the picture started by the nanosecond experiments.

It is useful to discuss the picosecond dynamics one would expect for the two cases where the transient grating amplitude responsible for Bragg-diffraction of the signal beam originates from either the photoinduced singlet exciton density or the triplet exciton density that is formed by fission. The lifetime of singlet excitons is expected to be at least several picoseconds, and therefore a signal proportional to the singlet density would build up during the laser pulse, as molecules are promoted from the ground state, followed by a decay during several picoseconds as the singlet exciton density decreases because of the fission process. On the other hand, triplet excitons would be formed through this fission process, and therefore they would lead to a diffracted signal that builds up after the end of the excitation pulses, reaching a quasi steady-state before a decay as described in the previous chapter.

How the diffraction efficiency builds up will identify which of the two possible states we are detecting. Diffraction from a grating created by the singlet excited state would imply we are sensitive to a deposition of energy into the sample, therefore our data should show a step function that builds up within the 1 ps pulse width as the ground state singlets are promoted to an excited state. This would then be followed by a decay of the signal as the singlets disappeared due to fission into triplets.

Diffraction from a grating created by the triplet excited state would imply we are sensitive to the singlet fission process that creates the triplets. In this case the data would show a delayed build-up that reaches a quasi steady-state before it decays, e.g. via the bimolecular recombination process discussed in the previous chapter. The delayed build-up should be completed in a time comparable to the reported time that is required for singlets to undergo fission, somewhere in the range of 2-20 ps [33, 52, 54, 55], allowing us to observe the gradual creation of a population of triplets as singlets undergo fission.

In this chapter, we will use pump and probe transient grating experiments on a time scale between 1 ps and 15 ps to focus on the build-up dynamics of the excitation that was investigated in Chapter 4. This is important in order to test the idea that was discussed earlier that the grating amplitude generated at 532 nm was due to triplet excitons. If this is the case, then the signal discussed in Chapter 4 should build up *after* the end of the excitation pulse.

5.1 Experimental Details

Chapter 4 showed the first transient grating pump and probe investigation of exciton dynamics in the rubrene single crystals on the nanosecond time scale, focusing on the decay dynamics and the effect of bimolecular interactions. Performing the pump and probe transient grating experiments on the picosecond time scale using 1 ps

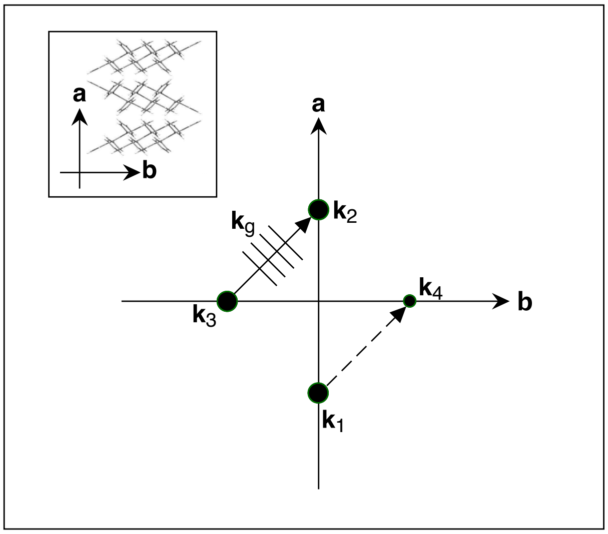

Figure 5.1: A projection onto the *ab*-plane of the crystal of the interacting beams' wavevectors in the transient grating set-up. The green dots are at the coordinates of the tip of the individual wavevectors on a coordinate plane parallel to the crystal's surface. Inset: Rubrene's *ab*-plane, for reference.

duration laser pulses will allow us to determine the state that generates our grating by observation of the signal dynamics after excitation.

The laser used in the forward facing configuration discussed in Chapter 2 produces a beam of pulses at 775 nm. This beam is used to pump the TOPAS optical parametric amplifier, which creates wavelength tunable pulses by second order nonlinear optical effects. In this chapter we will present data obtained at a wavelength of 532 nm, chosen to match the wavelength used in the experiments detailed in Chapter 4. At this wavelength the full-width at half-maximum ($FWHM$) of the laser pulse is ~ 1.12 ps, as determined by Eqn. 2.15 with a time constant for the data of $\tau = 0.83$ ps obtained from the Gaussian instantaneous response of a reference material.

The output beam from the TOPAS passes through beam splitters, producing three beams that are focused at the sample with beam waists of $\sim 600\mu$m and peak energies of $\sim 2\mu$J. The peak intensity of each beam is therefore 1.7×10^{12} Wm^{-2}. The excitation pulses crossed at a fixed angle of 4.8° between the two beams,

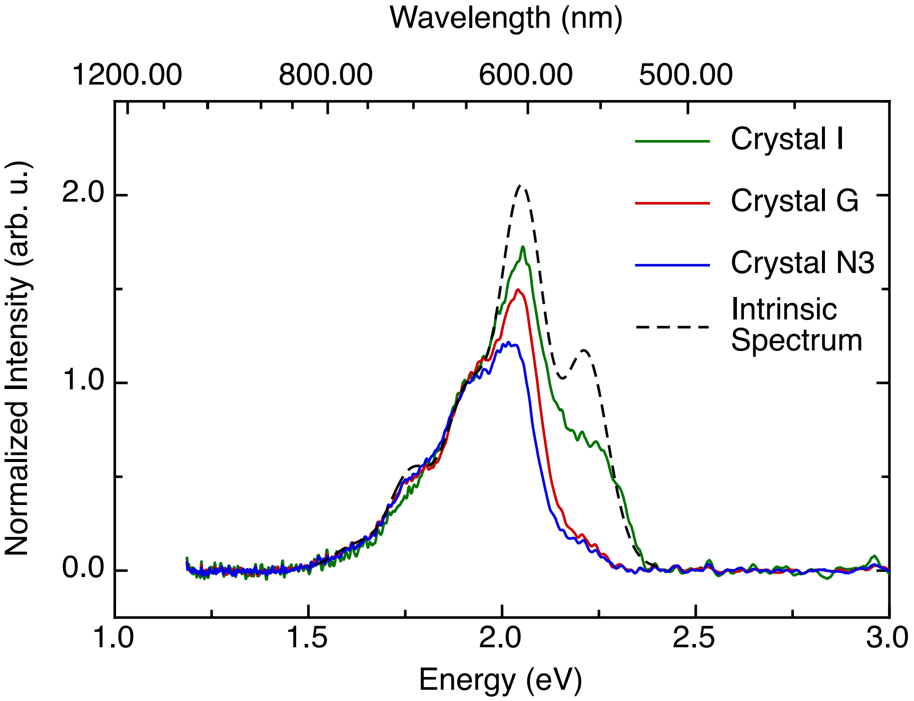

Figure 5.2: Photoluminescence intensities for polarization along the a-axis from samples G, N3, I, and the intrinsic PL of rubrene obtained by Ref. [43], all normalized to the shoulder at ~ 650 nm.

creating a transient grating with a spatial period of 6.4 μm. The transient grating was detected by measuring the diffraction efficiency of a time-delayed pulse incident under the Bragg condition. The diffracted pulse was detected by a photomultiplier tube (PMT) whose output voltage was integrated by a boxcar integrator over a 20 ns time-interval defined by the gate width, and then averaged over multiple repetitions to produce a clean, clear data set.

5.2 Crystal Samples Used in the Experiments

Three single crystal samples were chosen for detailed study to confirm reproducibility of the results. The samples used had dimensions of ~ 1 mm along the a and b directions and 10 - 12 μm along the c direction. The crystals were mounted such that the excitation light was a-polarized, as in Chapter 4, to produce the strongest

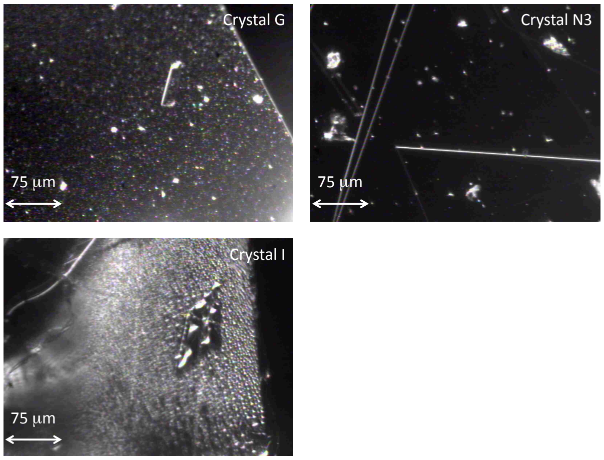

Figure 5.3: Images taken with a 20x objective of typical surface features of Crystal G, I, and N3, the three samples selected for study.

signal. Due to the forward facing configuration, the grating wavevector $\mathbf{k_g}$ was created at an angle of 45° in the plane defined by the a- and b-axes (see Fig. 5.1). Similar to the experiments described in Chapter 4, we confirmed that variation of the direction of the grating wavevector did not affect the observed transient grating dynamics.

The quality of each sample was determined by its individual photoluminescence (PL) emission spectrum taken from the ab-plane for light polarized along the a-axis. Fig. 5.2 shows that all three samples exhibit a peak at 610 nm, with smaller shoulders at other vibrational states (such as at 650 nm) and minimized scattering of c-polarized light at 564 nm, indicating all samples were pristine rubrene crystals [43]. Of note is sample I, which shows an enhanced shoulder around 560 nm, indicating that there is scattering by c-polarized light traveling through the crystal and leaking out through cracks and defects in the sample.

Fig. 5.3 shows the surface features for the three samples analyzed over an area of 900 μm^2. There are variations in severity of defects present. Sample I stands out among the samples as having many defects on its surface, providing more facets for c-polarized light to leak out.

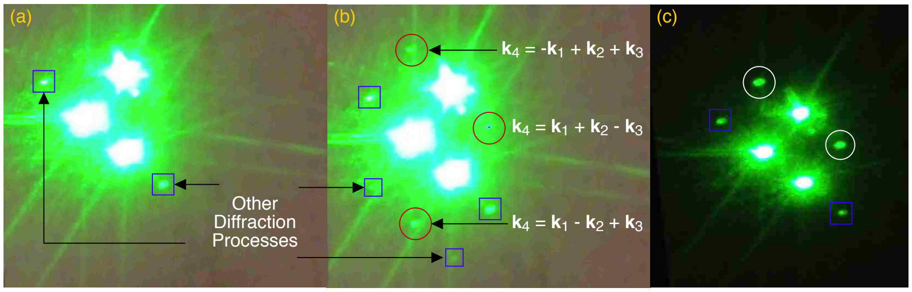

Figure 5.4: Examples of Bragg, Raman-Nath and self-diffraction. Panel (a) shows the transmitted pump and probe beams at $t = -10$ ps. Panel (b) shows the transmitted and radiated pulses at time $t = 0$ ps. Panel (c) shows the beams diffracted by the transient grating for $t = 50$ ps. The beams created from Bragg and Raman Nath diffraction are indicated with circles in panels (b) and (c). The radiated pulse $\mathbf{k_4} = \mathbf{k_1} + \mathbf{k_2} - \mathbf{k_3}$ is the detected signal. Spots due to self-diffraction are indicated by squares in all three panels.

5.3 Main Features of the Photoinduced Grating Dynamics on the Picosecond Time Scale

To exemplify how the transient grating experiment was realized for this forward facing experimental configuration, we show in Fig. 5.4 several photographs of the transmitted laser beams and of the diffracted laser beams for times before, at, and after time coincidence of the probe beam with the pump beams. In panel (a), two beams that result from self-diffraction of the two interfering pump pulses are present when the probe pulse reaches the sample before the pump pulses. The self-diffracted beams are boxed in blue. In panel (b), the appearance of several diffracted beams is apparent at time zero. The Raman-Nath and Bragg-diffracted signals are circled in red, where the phase matched beam occurring at $\mathbf{k_4} = \mathbf{k_1} + \mathbf{k_2} - \mathbf{k_3}$ is the beam monitored in this chapter. Panel (c) shows the strong diffracted signals from the transient grating, visible when the probe pulse reaches the sample a few picoseconds after the pump pulses.

The detected signal becomes visible, much more so than at time zero, as the amplitude of the grating gets stronger, implying that it takes some time to build up. The very visible signal can be seen in Fig. 5.5 for $t = 50$ ps. The phase matched

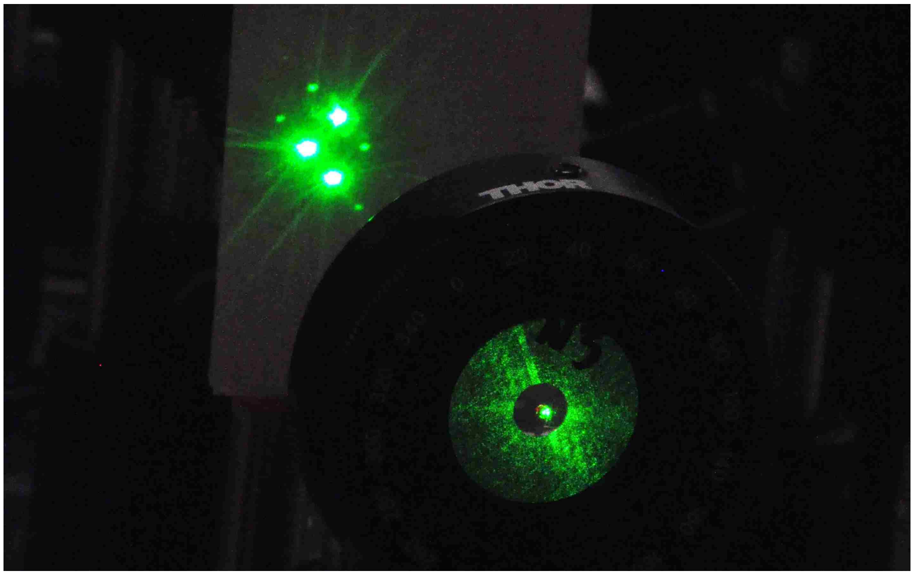

Figure 5.5: Mounted rubrene sample in foreground where the beams meet, and a screen in the background where the transmitted and diffracted beams, in the characteristic formation, are seen for delay time $t = 50\,\text{ps}$.

signal is seen at the far right corner of the square created by the transmission of the (much brighter) pump and probe pulses. Also visible in Fig. 5.5 are the self-diffracted two-beam interactions that can occur after time zero and the non-Bragg-matched beam at the top.

Fig. 5.6 shows the typical time dependence of the diffraction from the photoinduced grating for the three single crystal rubrene samples selected for study. The signal was detected by measuring the energy of the pulse at location $\mathbf{k_4} = \mathbf{k_1}+\mathbf{k_2}-\mathbf{k_3}$ in Fig. 5.4. The diffraction efficiencies in Fig. 5.6 have been normalized to the peak corresponding to the instantaneous response at a delay of zero in order to better visualize the data, as several details of the experimental set-up can influence the amplitude observed in the experiment. It is expected that the influence is the same for all components of the response.

Two main features stand out in these data: a slight protuberance at a delay time of zero and an exponential build-up that levels to a plateau after a few picoseconds. The protuberance at time t = 0 ps can be seen to varying degrees in the samples

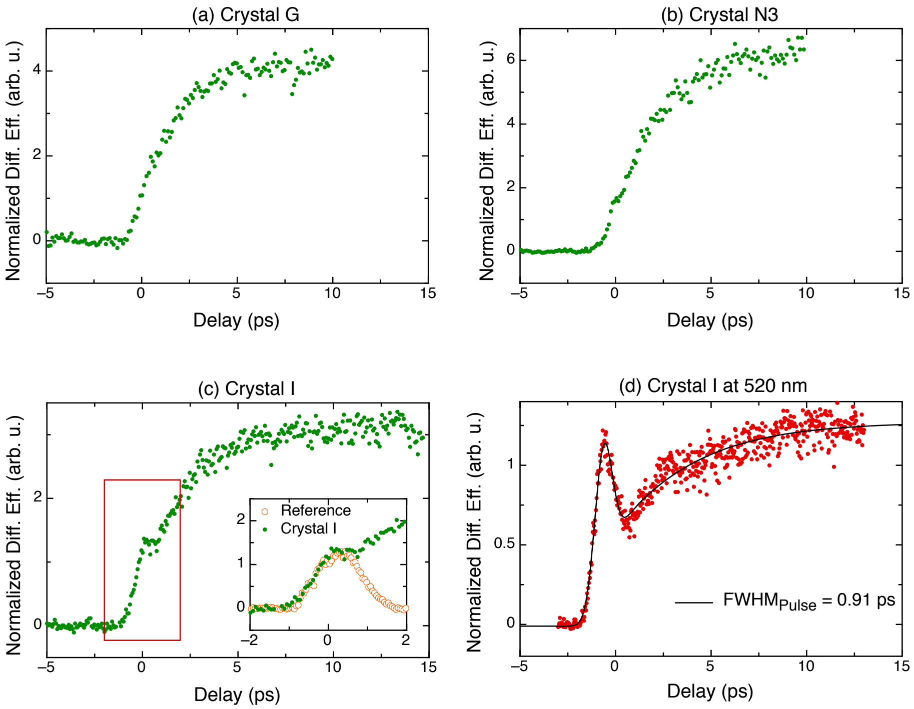

Figure 5.6: Example of the build-up in three different rubrene single crystal samples; G, N3 and I. A quasi steady-state is reach within 10 ps for all samples studied. Inset to (c) shows greater detail of the third-order instantaneous response superimposed with the response of a reference sample taken at 532nm. (d) shows the instantaneous peak of sample I at 520 nm.

shown, and corresponds to the instantaneous third-order nonlinear optical interaction off the three laser pulses arriving at the same time in the crystal. The inset in panel (c) of Fig. 5.6 shows in greater detail the instantaneous response in sample I overlaid with a similar signal profile obtained at 532 nm from a reference sample that shows an instantaneous peak.

Panel (d) of Fig. 5.6 shows a much more pronounced instantaneous peak seen in sample I in a different experiment where the wavelength of the TOPAS output was tuned to 520 nm. In section 5.4, it will be shown that the peak at time zero is indeed caused by the instantaneous third order response of the sample. The $FWHM$ of the peak as determined by the fit of the parameter τ_{Inst} ps in Eqn. 2.14 results in a $FWHM$ for the data of 0.67 ps and a $FWHM$ for the laser pulse of 0.91

ps. These results match with what is expected at that wavelength based on other measurements. A more detailed discussion of this issue is given in Chapter 6.

The signal from the instantaneous response is then followed by an exponential growth that increases until it reaches a plateau. The plateau reached is always larger than the peak at zero caused by the instantaneous response. When the peak at zero is not visible, the grating amplitude exhibits exponential growth starting at the initial excitation time t = 0 ps, and continues to increase until it reaches the plateau.

A rough qualitative analysis shows that the time required to reach the stationary final value of the amplitude differs slightly from sample to sample, but in each case approximately 40% of a quasi steady-state is achieved within 3 ps. The quasi steady-state is maintained for over a time scale of 100 ps (see Fig. 6.6 in Chapter 6, panel (a)).

The completion of the growth of the signal within 10 ps is consistent with the immediate build-up occurring within the 20 ps pulse length reported in Chapter 4. From Chapter 4, we know the signal is maintained until the excited states start to decay via bimolecular recombination at a rate dependent on the initial excitation density. Experiments in this chapter were performed at total fluences less than 25 J/m^2, resulting in excitation densities lower than 4×10^{18} cm^{-3}, densities much lower than those investigated in Chapter 4. We therefore do not anticipate detecting a large bimolecular effect in these data on the picosecond time scale. This is confirmed by the absence of any decay in the three samples studied for the time scale analyzed.

5.4 Analysis of the Transient Grating Dynamics

The time dynamics across the samples selected for study consistently showed a quasi steady-state that is reached within 10 ps, with variations in the visibility of the instantaneous nonlinear response at a 0ps delay of the probe. Recall that for an instantaneous third order response, the *FWHM* of the detected signal is directly related to the *FWHM* of the laser pulse. The *FWHM* of the peak at time zero seen in samples N3 and I is exactly what would be expected from the pulse duration at 532 nm. This correlation gives evidence that the peak is a result of the instantaneous third-order response of the sample.

Panel (c) of Fig. 5.6 clearly shows the correlation of the width of the third-order instantaneous responses seen in both rurbene and the reference sample. The instantaneous response of both the rubrene sample and the reference sample have full-width at half-maxima of ~ 1.38 ps, verifying that the peak at zero seen in rubrene is indeed the instantaneous third-order response..

The third-order instantaneous process is always present. It is a result of the time confluence of the probe pulse with the two excitation pulses. It then becomes important to determine why the peak at zero does not appear uniformly throughout the samples. In some samples the peak is masked by the build-up of the triplet state.

We believe the inconsistency of the third order nonlinear response's visibility among samples to be a result of the fission process being affected by some individual characteristic of the sample rather than a result of the instantaneous response changing from sample to sample. This is confirmed by the diffraction efficiency measurements which show that, when visible, the instantaneous peak is roughly the same size across many experiments. We can therefore normalize the data to keep the size of the instantaneous response the same by dividing each data set by the amplitude of the peak at zero. The measured diffraction efficiencies for the instantaneous third order responses for each sample were roughly the sample, justifying normalization to the peak at zero.

What is consistent from sample to sample is a quasi-steady state amplitude that is reached within 10 ps and is larger than the amplitude of the instantaneous nonlinear response. A quantitative evaluation of the evolution of the exponential build-up can be achieved by fitting the diffraction efficiency, η, to the square of an exponential build-up function,

$$\eta = \left(A_{Delay}\left[1 - e^{-(t/\tau_{Delay})}\right]\right)^2 . \tag{5.1}$$

A_{Delay} is the quasi-steady state amplitude attained once the grating has built up, and τ_{Delay} is a time constant that indicates how long it takes for the amplitude to achieve 40% of its quasi-steady state value. At an excitation of 532 nm, we obtain $\tau_{Delay} = 3 \pm 1$ ps across all samples.

We clearly see that, at an excitation of 532 nm, the photoexcited singlets undergo the fission process, and produce a large population of triplets in a few picoseconds. The build-up time within ~ 10 ps for our signal matches well with earlier observations of transients assigned to the formation of triplets by fission [33, 52, 54, 55]. The signals do not show an immediate response that reaches a maximum within 1 ps and decays later in any of the samples observed, as would be indicative of detection of the singlet state.

These results confirm our assignment of the build-up and decay of the transient grating at 532 nm as the variations of the grating amplitude caused by the creation of triplet states via fission, followed by a density-dependent decay that is governed by bimolecular interactions, as discussed in the previous chapter.

Chapter 6

Transient Grating Spectroscopy

A wavelength of 532 nm initially promotes a rubrene molecule to the ground vibrational state of the first electronic excited state, in a singlet configuration. Chapter 4 described our measurement of the decay of that grating, which is due to bimolecular recombination of either independent triplets or the quantum superposition of a triplet pair and a singlet state. In Chapter 5 we showed that, at this wavelength, the detected grating amplitude must be related to the creation of two triplet states from fission of the singlet. It is now of interest to determine what is the effect of the singlet exciton being promoted to a higher vibrational state.

It is reasonable to expect that different processes occur at higher vibrational states, and that photoexcitation to higher vibronic states affects both fission and the creation of free charge carriers [32, 46]. Since we know the energies of the higher vibrational states we can judiciously select wavelengths to perform wavelength dependent experiments on a picosecond time scale. With these experiments we can monitor the progression of processes that occur as the state reached after photoexcitation moves away from the ground vibrational state and to higher vibrational levels of the rubrene exciton.

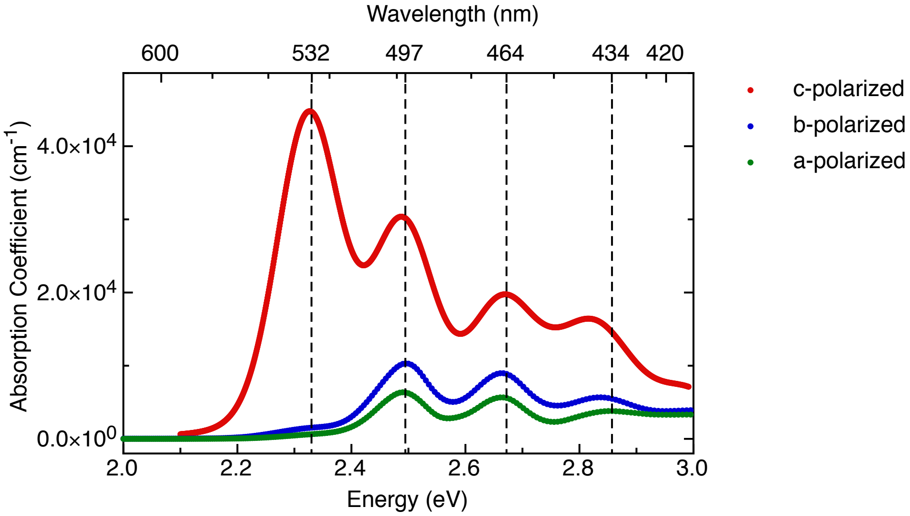

Figure 6.1: The absorption coefficients for light polarized along the *a*-, *b*-, and *c*-axes of rubrene crystals [43]. The dashed lines represent the excitation wavelengths used in the experiments described in section three of this chapter: 434nm, 464nm, 497nm and 532nm.

6.1 Choice of Excitation and Detection Wavelength

Figure 6.1 shows a close-up view of the absorption spectra from Fig. 3.3 obtained in Ref. [43] for rubrene single crystals when the light was polarized along either the *a*-, *b*- or *c*-axes of the crystal. The spectrum shows absorption peaks at 2.32 eV, 2.49 eV, 2.66 eV, and 2.83 eV (wavelengths 532 nm, 497 nm, 464 nm, and 434 nm, respectively). There are many vibrational modes in a molecule as large as rubrene. The 0.17 eV separation has been assigned to the energy difference between a specific subset of the vibrational modes [62]; a subset that is mostly related to vibrations that make C-C bonds oscillate in length at a high frequency close to 1300 cm^{-1} [63].

The photon energies 2.32, 2.49, 2.66 and 2.83 eV correspond to the ground, first, second and third vibrational states of the first excited state singlet in rubrene single crystals [43] (see Fig. 6.2). We may therefore use these energies as the excitation and detection wavelengths to observe how the singlet fission process progresses when the molecule is promoted to a higher vibronic state than that produced by excitation at 532 nm. It is important to recall at this stage that, because of constraints of the

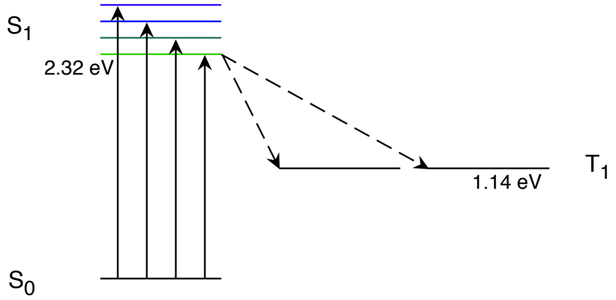

Figure 6.2: Energy levels of the singlet and triplet states. The vibrational states in the first excited singlet are separated by 0.17 eV. The solid arrows represent excitation and the dashed arrows represent fission.

experimental set-up, varying the wavelength of the excitation pulses automatically varies the wavelength of the probe pulse.

6.2 Experimental Details

The laser and set-up for the experiments performed at varying wavelengths are identical to those used in the picosecond transient grating experiments at 532 nm described in Chapter 5. However, a small number of experimental conditions are different when varying the wavelengths. In order to account for the change in energy when the wavelength is varied, the energy per excitation pulse was kept at roughly $\sim$1 μJ for each wavelength by use of neutral density filters.

The pulse length varied slightly with changing wavelength. Figs. 2.7 and 6.3 show the instantaneous response from a reference sample when the laser is tuned to some of the wavelengths used in this investigation. These data show the result of the correlation measurement as obtained in degenerate four-wave mixing when varying the delay of one of the interacting pulses. Table 6.1 shows time constants obtained from a fit of the data to Eqn. 2.13 and the corresponding $FWHM$s.

The beam waist of the input beams is also different for different wavelengths, with individual waists of $\sim$ 900 μm at 497 nm, $\sim$ 850 μm at 464 nm, and $\sim$ 700

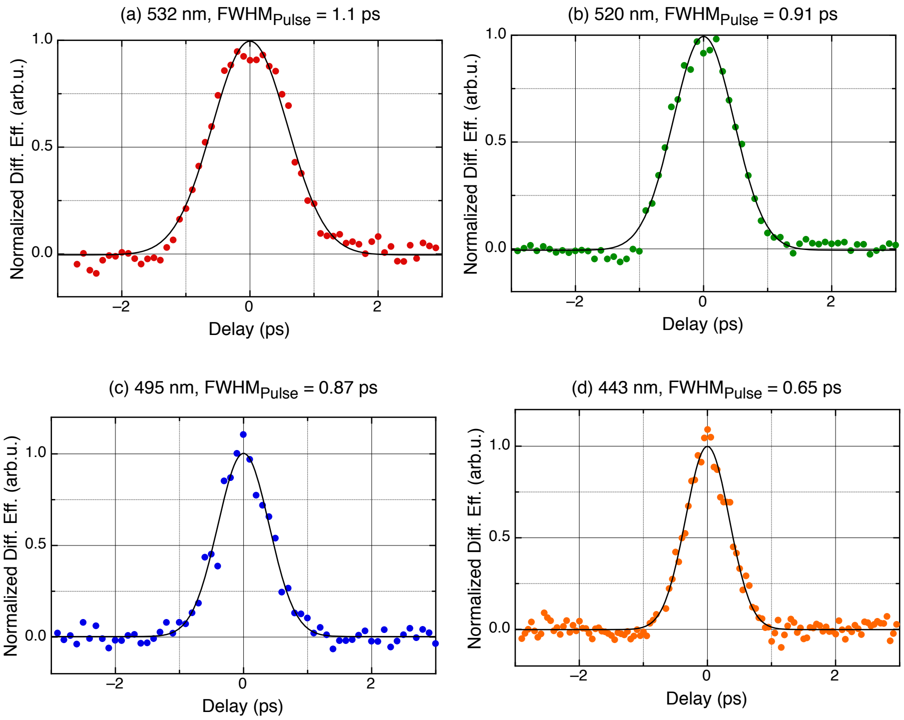

Figure 6.3: Examples of the third-order nonlinear response in a reference sample with a profile dependent on pulse width (which changes with wavelength) of the TOPAS optical parametric amplifier output.

μm 434 nm. Finally, because part of the probe beam's path travels through glass mounted on the retroreflector, and because the speed of light in glass is frequency dependent, changing the wavelength changes the time required to traverse the glass. Therefore the probe's time delay had to be adjusted to find the appropriate $t = 0$ ps required to achieve temporal overlap between the pump and probe pulses inside the crystal.

6.3 Typical Wavelength-Dependent Transient Grating Dynamics

In this chapter we will investigate the build-up dynamics while using different wavelengths for excitation and detection. The experiments at different wavelengths will

Table 6.1: Determination of the *FWHM* of the detected signal, and therefore of the laser pulse, as determined by the fit parameter τ_{inst} for various wavelengths.

Wavelength (nm)	τ_{inst} (ps)	FWHM$_{Inst}$ (ps)	FWHM$_{Pulse}$ (ps)
532	0.82	1.4	1.1
520	0.67	1.1	0.91
495	0.64	1.0	0.87
460	0.51	0.85	0.69
443	0.48	0.80	0.65

show that the build-up consists of three independent components: an instantaneous one that gives a gaussian peak at a time delay of zero, a step-like one that corresponds to the effects of energy deposition into the material, and a delayed build-up that matches what we have seen in Chapter 5.

These three features can be described as a function of time in order to parameterize the data obtained by excitation to higher vibrational levels of the excited state singlet. We model the observed diffraction efficiency with a function that is a combination of these three components: the step increase due to deposition of energy into the crystal during the pulse length, the peak at a delay of zero due to the instantaneous nonlinear response, followed by the delayed exponential build-up to a quasi steady-state of the grating amplitude. We therefore have,

$$\eta \propto A_{Inst}(t) + \left[A_{Step}(t) + A_{Delay}(t)\right]^2 , \tag{6.1}$$

where A_{Inst} represents the instantaneous response, A_{Step} is the step-like feature representing a grating written by the energy deposited in the sample while the pump pulses are present in the sample, and A_{Delay} represents a a grating that grows exponentially at a later time. A_{Inst}, A_{Step}, and A_{Delay} are given by

$$A_{Inst}(t) = A_{Inst}(0) e^{-(t/\tau_{Inst})^2} \tag{6.2}$$

$$A_{Step}(t) = A_{Step}(0)\left(1 + erf(t/\tau_{Inst})\right) \tag{6.3}$$

$$A_{Delay}(t) = A_{Delay}(0)\left(1 - e^{-(t/\tau_{Delay})^2}\right) . \tag{6.4}$$

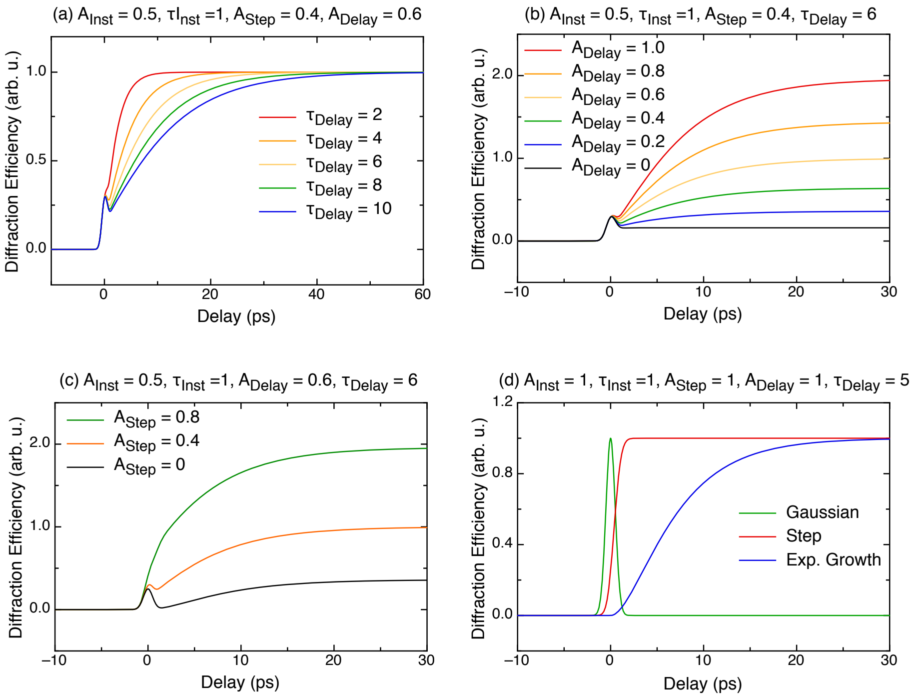

Figure 6.4: Examples of how the parameters effect the time dependence of the data. Plots showing the affect of varying (a) the time constant of the delayed build-up, (b) the amplitude of the delayed build-up, and (c) the amplitude of the step. (d) shows the three components separately.

Here, $A_{Inst}(0)$ is the maximum signal reached by the instantaneous peak, τ_{Inst} is the time constant of the peak, same as the time constant discussed in Chapter 2 that leads to the $FWHM$. $A_{step}(0)$ represents the amplitude of the step-like function. $A_{Delay}(0)$ is the maximum amplitude of the delayed build-up, and τ_{Delay} is the time constant that indicates how much time is required to reach $(1 - e^{-1})^2 = 40\%$ of the quasi steady-state. Fig. 6.4 shows the general shape of this description when the various parameters are varied.

The form for the instantaneous response has been described in section 2.4.1 on page 17. We have found experimentally that the best fit to the data is obtained when one assumes that the two gratings associated with step-wise and delayed build-up, respectively, are in phase. Hence, their two contributions are first added, and then squared to obtain the energy of the diffracted probe pulse. On the other hand, we have found that the data is best described if the intensity of the signal caused by the instantaneous response is simply added to the intensity caused by diffraction from the step-wise and delayed gratings. This means that we assume that the instantaneous response is approximately out-of-phase by 90° with the step-wise response, as determined by the third-order susceptibility described in section 2.4.1.

Recall from Chapter 2, Eqn. 2.14 that the time constant of the detected signal and of the laser pulse that causes the response are related by $\tau = \sqrt{\frac{2}{3}}\tau_{Inst}$. From a fit to the τ_{Inst} parameter in Eqn. 6.2, the $FWHM$ of the laser pulse is given by $FWHM = 2\tau\sqrt{\ln 2}$. Therefore the τ_{Inst} used in Eqns. 6.2 and 6.3 is related to the duration of the laser pulse, however it is measured.

The instantaneous response at a delay of zero serves as a good reference for comparisons between signals. In Chapter 5 we were concerned with the consistency of the response while changing samples. In this chapter, we are concerned with the consistency of the instantaneous response while repeating the experiment at differing wavelengths. While the absolute strength of the signal detected in the transient grating experiment depends on the quality of the alignment and adjustment of the overlapping beams, on the energy of the interacting pulses, and also on other aspects such as the quality of the sample at the position where the transient grating is written and detected, all these factors affect the instantaneous response as well as the step-wise and delayed responses in the same way. Therefore, below we will eliminate any dependence of the signal from difficult to control factors by normalizing everything to the strength of the instantaneous response. By comparing absolute diffraction efficiencies between wavelengths we have established that the strength of the instantaneous response has only a weak dependence on the wavelength when compared to the observed changes in the strength of the delayed response, which are much stronger.

Fig. 6.5 shows a close up on the fit of the peak at time zero for excitation at 460 nm. As the build-up of the quasi steady-state amplitude becomes slower, the instantaneous peak becomes less and less masked by the other transient grating contributions. This allows for the accurate fitting of the instantaneous response,

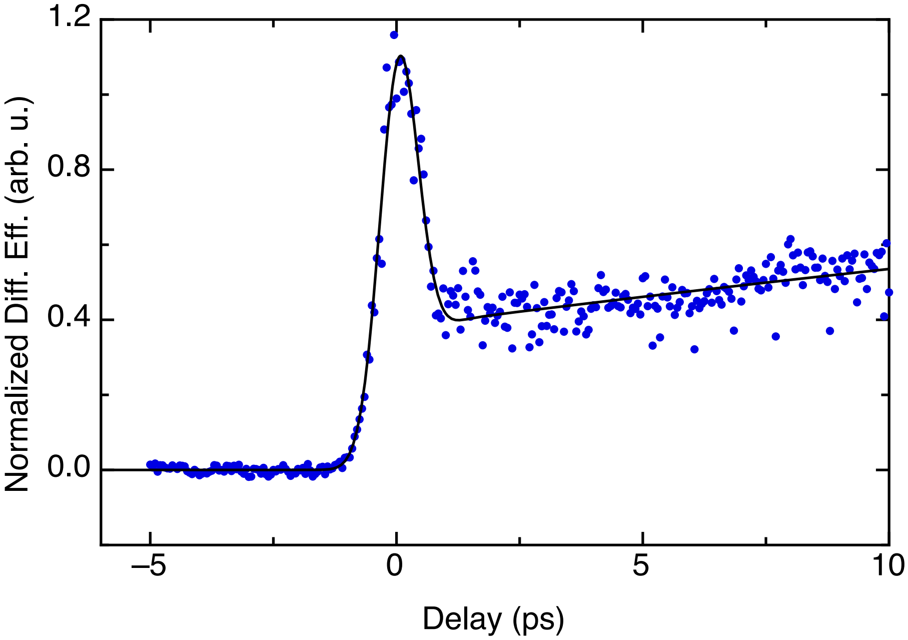

Figure 6.5: Expansion of third order instantaneous response near a delay of 0 ps for excitation at 460 nm. Fit to this peak returns a *FWHM* for the signal of 0.92 ps, compared to 0.85 ps in the reference sample.

which forms a peak at a delay of zero. The time constant τ_{Inst} returned from the fits consistently matched with those obtained for the reference sample shown in Figs. 2.7 and 6.3, verifying that the peak is the result of a third order process for all wavelengths investigated.

Finally, note that Eqns. 6.2 and 6.3 have the same ratio inside the exponential and inside the error function, respectively. This is because the error function is defined as the integral of the gaussian in Eqn. 6.2. The relationship between Eqns. 6.2 and 6.3 can also be understood by a thought experiment involving a simple situation where light absorption leads to excitation to a higher state that has a lifetime either much shorter or much longer than the laser pulse length. When the lifetime of the excited state is shorter than the pulse length, the number of excited states will be proportional to the intensity of the light. This would be seen in the data as a Gaussian. If the lifetime of the excitation is longer than the pulse length for the time scales investigated, the number of excited states will be proportional

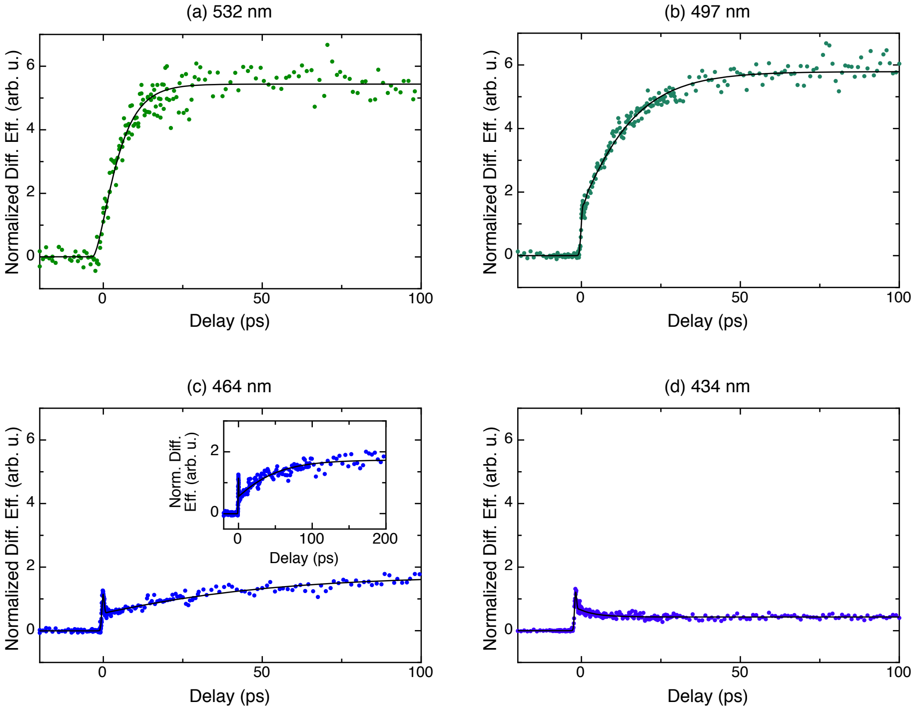

Figure 6.6: Transient grating dynamics at excitation energies near the absorption peaks at a grating spacing of 6.4 μm. Pulse energies of beams 1, 2 and 3 are 0.6, 1.2 and 1.1 μJ, respectively. Inset to (c): longer time scan at 464 nm to show build-up to full quasi steady-state amplitude.

to the integral of the intensity. This is seen as a stepped increase in the data. Therefore Eqn. 6.3 describes what would happen to a grating that is created by the instantaneous energy deposition from the laser pulses when the excitation lifetime is longer than the laser pulse length.

6.4 Excitation at the Absorption Peaks

In this section we first present results of experiments performed using excitation and detection light at wavelengths corresponding to the main absorption peaks in the absorption spectrum of rubrene. Measurements made with excitation energies at and around the absorption peaks have been repeated many times to test for reproducibility. Figs. 6.6 and 6.7 show the typical results we obtained.

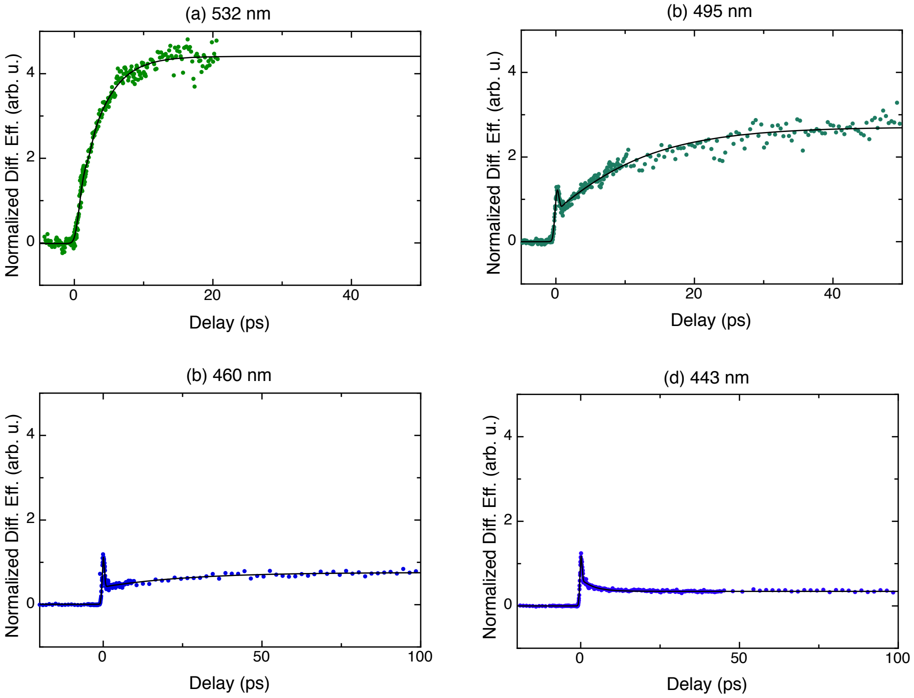

Figure 6.7: Transient grating dynamics at the same four wavelengths as in Fig. 6.6, taken under slightly different experimental conditions and at another location in the sample. Pulse energies: 0.8, 2.8 and 1.3 μJ. Grating spacing: 6.4 μm.

The diffraction efficiencies were determined by taking into account the excitation energies, sample thickness and the wavelength dependent absorption coefficients (as described by the attenuation factor A_α in Eqn. 2.18), revealing little variation in the amplitude of the peak at time zero. We therefore normalized to this peak amplitude to better visualize individual features of the data.

In these examples, the instantaneous third-order response seen at time t = 0 ps and a *delayed* exponential build-up to the quasi steady-state triplet population become much more visible. Note that the data presented are those of the normalized diffraction efficiency of the grating, which is proportional to the square of the amplitude of the grating. All fits to the data were performed for the amplitude, and therefore yield parameters, such as the build-up time constant, that are for the amplitude and not for the diffraction efficiency.

Panel (a) in Figs. 6.6 and 6.7 shows the familiar build up for an excitation at 532nm. As was seen in the build-up at 532 nm seen in Chapter 5, fitting the data to Eqn. 6.1 gives a time constant of 3 ± 1 ps, representing the time required to reach 40% of the quasi steady-state amplitude. Once the quasi steady-state is achieved it is maintained over the 100 ps time scale investigated. There is very little appearance of the third-order nonlinear response at time zero.

When exciting to higher vibrational levels, the delayed build-up that we assigned to the contribution of triplet excitons becomes less and less prominent and cannot be detected anymore when exciting to the highest vibrational level. As a consequence, the peak at time zero becomes much more visible at the higher excitation energies, and a step-like build-up also becomes evident. The step-like response corresponds to the energy deposited into the sample by the pump pulses while they are present in the crystal. The singlet population is also established during the same time, but if the detected signal was only caused by excited singlet states, then it would need to decrease with the same rate observed for the build-up of the triplet states, because we have shown earlier that initially photoexcited singlet states are converted into triplet states by fission. The origin of the step-like response observed at wavelengths between 440 and 460 nm will be discussed later in this chapter.

Panel (b) in Figs. 6.6 and 6.7 shows the diffraction from a grating created with excitation and detection wavelengths on the strongest absorption peak near 497 nm. Because the delayed exponential build-up is weaker, the peak at time zero caused by an instantaneous response, and also a step-wise buildup, start to be clearly visible. In Fig. 6.7, at an excitation of 495 nm, the peak at zero becomes much more visible as the build-up achieves a smaller quasi steady-state amplitude than when using 497 nm light to excite to the higher vibrational state. The delayed build-up takes longer to be completed than that at 532nm, with an average time constant of $\sim 10 \pm 4$ ps as determined by the description of Eqn. 6.1. Once the maximum amplitude is attained, the signal remains at that amplitude up to the nanosecond time scale.

It is clear in panel (c) of both Figs. 6.6 and 6.7 that when the excitation is at or near the absorption peak of 464 nm, corresponding to the second excited vibrational level of the C-C stretching mode, the quasi steady-state amplitude reached is quite small compared to that reached at other wavelengths. This leaves the instantaneous peak and the stepped increase quite visible, followed by a long build-up time that necessitated a longer scan to allow for the build-up to arrive at the quasi steady-state. The average time constant for excitations around 464 nm is $\sim 25 \pm 6$ ps.

We believe the discrepancy in final quasi steady-state amplitude for a given wavelength, which is observed when comparing Figs. 6.6 and 6.7, to be an artifact stemming from reproducibility issues. Inhomogeneities in the sample could have made the physical process responsible for the delayed build-up less strong in one experiment compared to the other. Therefore excitation and detection at different locations of the sample could result in the differences seen in Fig. 6.6 and 6.7. This sort of variability has also been seen in measurements at 532 nm, and slight differences in the quasi steady-state amplitude have been observed, but the dynamics of the build-up time remained remarkably consistent for all photoexcitation wavelengths.

Panel (d) of Figs. 6.6 and 6.7, showing data recorded around the peak at 434 nm, is where the most drastic change from data recorded at higher wavelengths is apparent. The complete lack of a delayed build-up leaves only the instantaneous peak and the stepped increase visible in the data. In fact, instead of a delayed build-up there is an exponential decay to a lower plateau with a time constant of 5 ± 1 ps. Similar to all other wavelengths studied, once a quasi steady-state is reached, it is maintained up to the nanosecond time scale.

The data obtained by measurements with excitation and detection energies around the absorption peaks are quite good, and can be fit very precisely with Eqn. 6.1. The feature of interest in these wavelength dependent measurements is the time required for the singlets to undergo fission to produce the triplet population responsible for the delayed exponential build-up in the diffraction efficiency. By decreasing the excitation wavelength, and therefore increasing the energy per photon used for excitation, the build-up time becomes longer, raising from 3 ± 1 ps to the 25 ± 6 ps observed when exciting with a photon energy near 2.67 eV. It then must be determined if lengthening of the build-up time is only a result of the fission rate slowing and requiring a longer time to complete the fission process – with the final fission efficiency essentially the same despite the slower build up – or if the change in amplitude of the delayed signal could also mean that the fission efficiency is decreasing.

It is quite reasonable to assume that the fission process can become slower, and yet still achieve a 95% fission efficiency – which we know is the case in rubrene. We will show below that it is more likely that the fission efficiency remains the same, and that the smaller amplitude of the delayed signal is instead connected to a decreased sensitivity to the triplet density because of the shorter wavelength used for detection.

6.5 More Detailed Spectroscopy of the Transient Grating

To paint a more robust picture of the changes in transient grating dynamics that occur between excitations at 464 nm and 434 nm that were described in the previous section, we performed measurements at incremental excitation energies between those corresponding to the absorption peaks. Fig. 6.8 shows how the shape of the build-up changes as the excitation energy is varied in small steps. Again, to better visualize individual features, all data have been normalized to the instantaneous third-order response at time zero.

The smooth transition from one curve to the next as the wavelength is changed confirms the previous results. We see that as the amplitude of the quasi steady-state decreases, and the time required to reach it increases. Therefore, the instantaneous response becomes more visible with decreasing wavelengths. We also observe that the width of the instantaneous peak decreases with decreasing wavelength, in accordance with the changing pulse length (see Fig. 6.3).

The data in Fig. 6.8 are shown in greater detail on individual axes in Fig. 6.9, confirming that the exponential build-up gradually disappears. The transition progresses from a clear build-up after a step-like deposition of energy at 460 nm (2.69 eV), to no discernible build-up after the step at 454 nm (2.73 eV), and finally

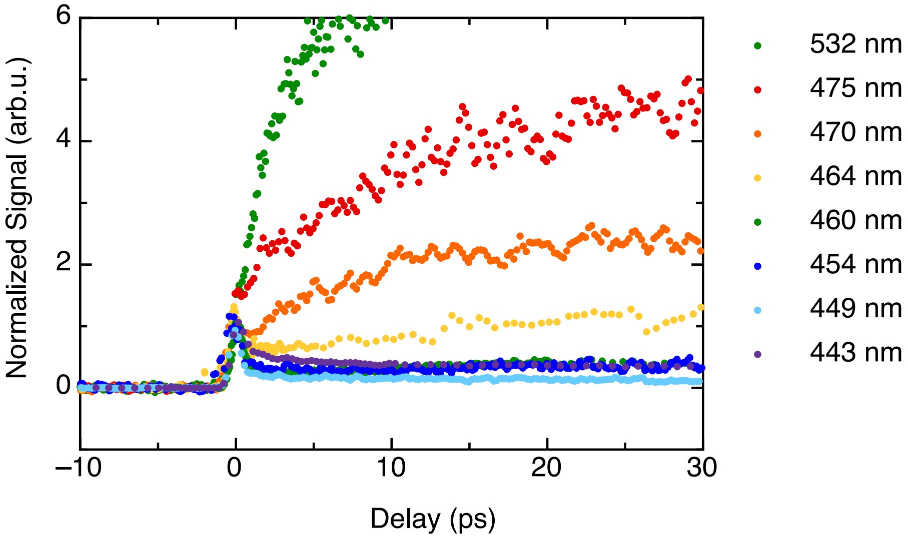

Figure 6.8: Wavelength dependence of transient grating dynamics. The delayed build up of triplets decreases in strength as the excitation energy goes above 2.7 eV (wavelengths below 460 nm). Above this energy limit, detection of the delayed build-up is impeded.

to a decay of the signal at 443 nm (2.79 eV). Fig. 6.9 also shows more clearly that the width of the instantaneous peak at time zero decreases with a decrease in wavelength.

All of the above observations can be summarized by plotting both the amplitude of the delayed exponential build-up and its build-up time as a function of wavelength. This is done in Figs. 6.10 and 6.11. Fig. 6.10 shows the build-up time vs. the photon energy used in the experiment. Fig. 6.11 shows the ratio of the delayed build-up amplitude to the amplitude of the third order instantaneous response. Above 2.73 eV, this trend become negative as we are no longer taking the ratio of a build-up amplitude to the instantaneous peak, but instead a ratio of a decay amplitude to the instantaneous peak.

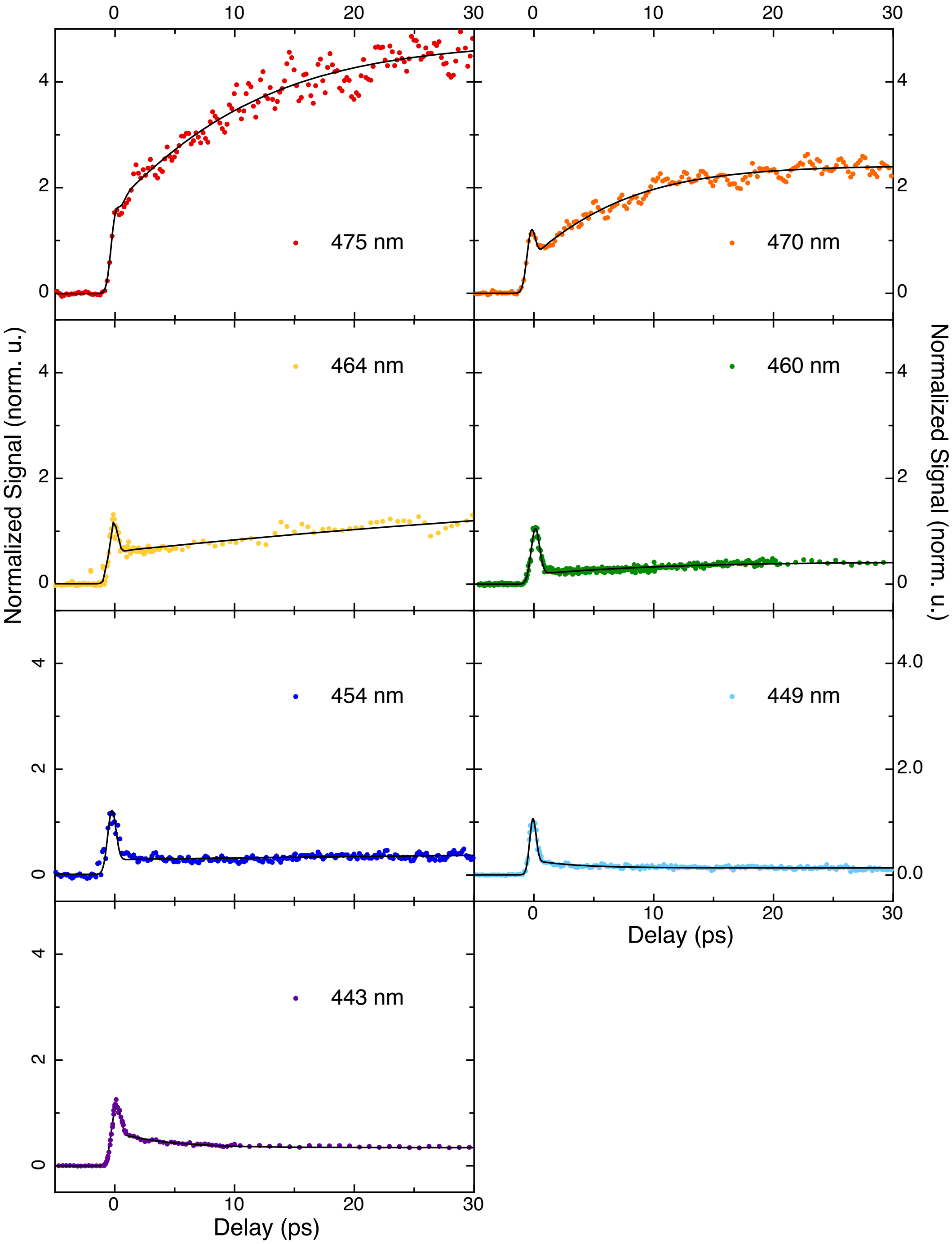

Figure 6.9: The measurements from Fig. 6.8 shown individually to see greater detail.

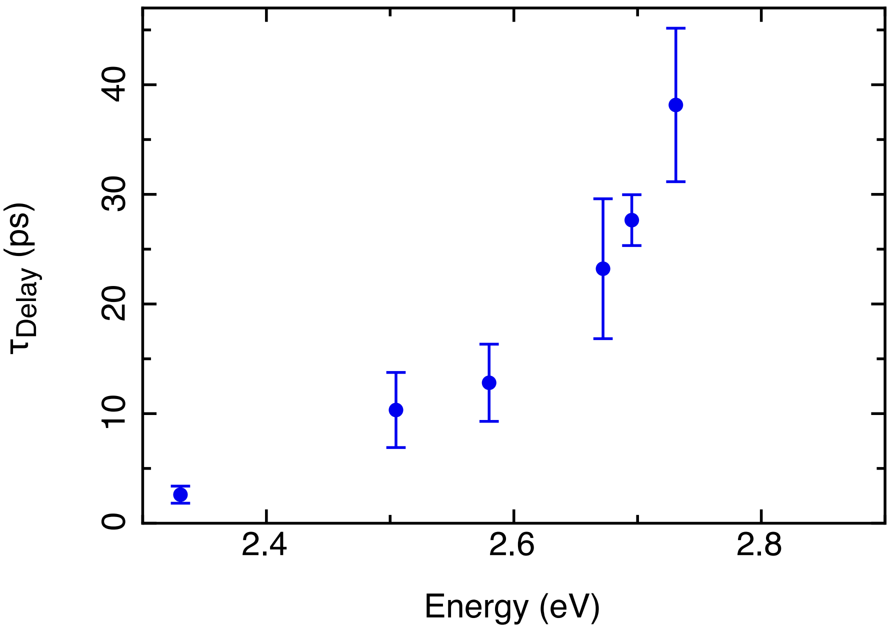

Figure 6.10: Energy dependence of the delayed build-up time constant.

6.6 Discussion of Spectroscopy Results

Our data have shown that sensitivity of the probe beam to the transient grating built by a population of triplets decreases with decreasing wavelength, and the build-up time required to create that grating increases with decreasing wavelength. We do not interpret the absence of a detected build-up during the first 200 ps at wavelengths below 460 nm as a sign that fission processes does not occur for these excitation wavelengths because there is ample experimental evidence that fission occurs efficiently at these wavelengths. Photoluminescence measurements performed at an excitation wavelength of 442 nm (2.80 eV) by Ref. [37] show that triplets continue to be generated, as evidenced by the visualization of triplet exciton diffusion along the *b*-axis. Therefore the observed disappearance of the delayed build-up that occurs at around 2.70 eV is not a result of a decrease in fission activity relative to that seen at excitations of 2.32 eV (532 nm).

The fact that our experiments become insensitive to triplets at shorter wavelengths should not have any influence on the detected dynamics, and the decreased

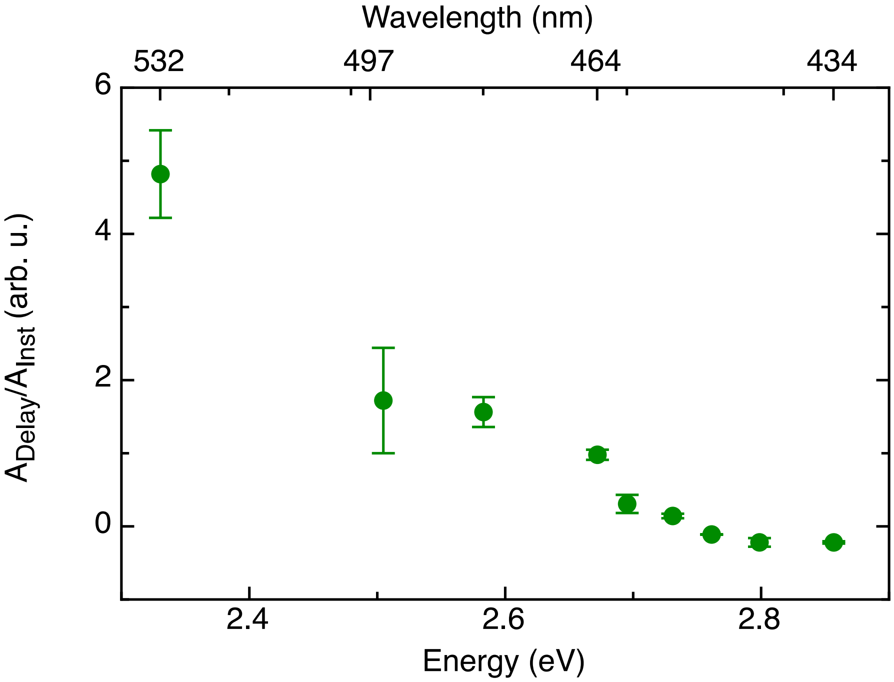

Figure 6.11: Energy dependence of the ratio of delayed build-up amplitude to the instantaneous amplitude.

build-up time at shorter wavelengths can still be seen as an indication of a slower (but equally efficient) singlet fission process. What is likely is that as we decrease the wavelength, the effect of a triplet on the complex refractive index seen at those lower wavelengths becomes weaker and weaker. Therefore the refractive index change detected by the probe pulse decreases, without necessarily indicating that the number of generated triplets decreases. Shorter wavelengths would simply be less sensitive to the presence of triplets.

The reason that the build-up time is longer remains a mystery. Fission must be occurring, as it is the main decay mechanism for the excited singlet state. It is just that the fission process necessitates a longer time when the initial photoexcitation also creates significant molecular vibrations.

Although we lose sensitivity to the delayed build-up, we remain sensitive to a step in the signal due to energy deposition at all wavelengths. The consistency of the step characteristic in our measurements could indicate that the step represents a ground state grating, that is a grating of the S_0 concentration, in which case we would always detect some signal. Note that an S_0 grating is not the same as an excited state S_1 grating, as S_1 can become two T_1 via fission while S_0 remains unchanged until the triplets recombine to S_1, which then relax back to S_0.

Recall from Chapter 3 that an instantaneous release of carriers was reported in photoconductivity experiments [42]. This photocurrent step could be correlated with the step characteristics in our transient grating experiments originating from an absorption or refractive index change caused by free electrons and holes.

There are currently conflicting interpretations of the physical mechanisms occurring at these low excitation wavelengths. Ma *et. al.* claim that an excitation at 444 nm produces a singlet-to-singlet transition, $S_1 \rightarrow S_n$ (see Fig. 4 of Ref. [33]). That is, an already excited molecule is promoted to a higher excited singlet state. Our data, viewed in conjunction with the PL data of Ref. [37], do not seem to support this claim. If the step characteristic had been due to a singlet state, the fact that fission describes a conversion between singlet and triplet states would have required a decay of the initial excitation on the same time scale in which the signal from triplet states increases.

A more reasonable interpretation of our data seems to fall in line with the interpretation of Tao *et. al.* , who report the creation of free carriers at an excitation wavelength of 450 nm. This claim is best illustrated in Fig 6. of Ref. [46]. This interpretation, considered along with the photoconductivity experiments of Ref. [42], seems a more likely explanation of the step characteristic in our measurements.

In this chapter we determined that decreasing the excitation wavelength (energy increased) increases the time required to reach a maximum triplet population, and that we are indeed sensitive to the triplet state in these transient grating pump and probe experiments from 532 nm to 460 nm. The build-up amplitude is reduced significantly as the excitation wavelength is decreased to 470 nm (2.64 eV), and the delayed triplet signal becomes very weak compared to the instantaneous nonlinear response. Once an excitation threshold of 454nm (2.73 eV) is surpassed, a delayed build-up is no longer detectable by our system.

In addition to the decrease in the amplitude of the delayed build-up, we also observed a systematic increase in its build-up time. We have also shown that the longer build-up time can be associated with a slower fission rate as the molecules are excited to higher vibrational levels. The decrease of the build-up amplitude, however, cannot be explained with a decrease of singlet fission efficiency, which must remain high. Because of this, we had to assign the decrease of the amplitude of the delayed build-up to a decrease in the coupling between the probe pulse and the triplet population as the wavelength of the probe pulse decreases.

The most surprising result of our experiments is the revelation that singlet fission takes longer when the initial excitation is to a higher vibrational level, with time constants of 3, 10, and 25 ps observed when exciting to the ground, first, and second vibrational state, respectively. It may be possible to argue that the fission time increases because fission always happens efficiently only from the ground vibrational state of the molecule, and that when exciting to higher vibrational states one first needs to wait for the molecule to relax back to the ground state before fission can occur. Assuming an average time of 7ps for relaxing from a higher vibrational state to the next lower one would be consistent with our results within the experimental uncertainty. However, a 7ps relaxation time from a higher vibrational state is much longer than the 1ps natural lifetime of higher vibronic states reported in Ref. [24]. Further research will still be needed in order to clarify the origin of the slower fission rate that we have observed.

Chapter 7

Conclusion and Outlook

The measurements that are presented in this work contribute detailed and accurate information on the processes with which photoexcited singlet excitons undergo fission to create triplet excitons.

For the first time we have been able to follow the dynamics of photoinduced excited states in rubrene using pump and probe transient grating experiments on the nanosecond and picosecond time scale. In particular, we observed a bimolecular interaction between excited states that can strongly affect the observed time dynamics on the nanosecond time scale, and has until now been overlooked both in time-resolved luminescence experiments as well as in photoinduced absorption experiments.

We have also shown through transient grating experiments on the picosecond time scale that the excited states that interact and decay on the nanosecond timescale are the triplets that result from singlet fission. This was determined by observing the build-up of the grating amplitude within the first 10 ps after excitation. This build-up corresponds to reported singlet-to-triplet fission times.

Transient grating spectroscopy experiments allowed us to observe the build-up of the grating amplitude as a function of the excitation energy. In these experiments we saw that as the excitation energy increased, the time required to reach a quasi steady-state amplitude for the grating increased, indicating that fission becomes slower. Although we lose sensitivity to this delayed build-up once the excitation energy surpasses 2.7 eV, we do consistently detect the presence of a step-like function in our data as the excitation energy increases. We interpreted this step as the presence of free carriers created fast dissociation of a small portion of photoexcited singlet states.

It is important to note that the conclusions presented here are our best hypotheses for a complicated system that requires further study. Recall that a singlet first transitions to a quantum superposition of the singlet state with two entangled triplets before two distinguishable triplets are produced. The 10 ps time has not yet been identified as that associated with the quantum superposition, or that of the individual triplets. This still needs to be determined, perhaps by tracking triplet movement or by analyzing the photoluminescence dynamics.

It is clear that much additional work will be required before a complete understanding of the singlet-to-triplet fission process in the rubrene single crystal is reached. It would be useful to improve on our ability to detect triplets as a function of excitation wavelength. Our current experimental conditions limit our ability to perform experiments that could improve triplet detection because the wavelength we used for detection was constrained to the same used for excitation, causing the probe pulse to lose sensitivity to the presence of triplet states. Probing with a wavelength different from that used to excite would allow the probe to remain sensitive to the presence of triplet states. A pump and probe transient absorption spectroscopy experiment could be one way of continuing the investigation of singlet fission by pump and probe experiments. A delayed white-light probe could be used to correlate the photoinduced changes in absorption at various wavelengths to the evolution of the excited state on the picosecond time scale.

Rubrene is one of the most promising organic semiconductors, but there are still many open questions regarding photoexcitation processes in this material. Further investigation of excited state dynamics in rubrene is necessary in order to gain more insights into the fission process that ultimately leads to two independent triplet excitons that are free to dissociate. It is hoped that this work will stimulate further work in the field by helping to clarify any inconsistencies in reported results due to the particular excitation density used or vibrational state being examined. We trust that the availability of these new data will allow researchers to properly design and interpret both photoluminescence and transient absorption experiments in rubrene, with the ultimate aim of painting an accurate picture of the processes by which a photoexcited singlet exciton creates triplet excitons, which ultimately can diffuse towards heterointerfaces and dissociate into charge carriers, a key process for organic photovoltaics.

Chapter 8

Haiklusion

Singlet to triplet.
My! How triplets recombine.
Went fishin', found fission.

Appendix A

Table of Q & ρ Values

Table A.1: Raman Nath parameters Q and ρ for transient grating experiments performed on the nanosecond time scale.

Wavelength (nm)	Grating Spacing (μm)	Q	ρ
532	0.376	166.7	147.0
532	0.388	156.5	138.0
532	0.390	155.0	136.7
532	0.567	73.3	64.7
532	0.588	68.2	60.2
532	0.592	67.3	59.4
532	1.42	11.7	10.3
532	1.61	9.06	7.99
532	1.74	7.79	6.87
532	1.84	7.00	6.17
532	1.92	6.37	5.82
532	3.07	2.51	2.21
532	3.32	2.14	1.89
532	3.58	1.84	1.63
532	6.33	0.588	0.519

Table A.2: Raman Nath parameters Q and ρ for transient grating experiments performed on the picosecond time scale.

Wavelength (nm)	Grating Spacing (μm)	Q	ρ
532	6.35	0.585	0.516
520	6.35	0.571	0.492
497	6.35	0.546	0.450
495	6.35	0.544	0.446
475	6.35	0.522	0.411
470	6.35	0.516	0.402
464	6.35	0.510	0.392
460	6.35	0.505	0.385
454	6.35	0.499	0.375
449	6.35	0.493	0.367
443	6.35	0.487	0.357
434	6.35	0.477	0.343

Bibliography

[1] Knupfer, M. Exciton binding energies in organic semiconductors. *Applied Physics A* **77**, 623–626 (2003).

[2] Reusswig, P. D., Congreve, D. N., Thompson, N. J. & Baldo, M. A. Enhanced external quantum efficiency in an organic photovoltaic cell via singlet fission exciton sensitizer. *Applied Physics Letters* **101**, – (2012).

[3] Congreve, D. N. *et al.* External quantum efficiency above 100singlet-exciton-fission–based organic photovoltaic cell. *Science* **340**, 334–337 (2013).

[4] Lee, J. *et al.* Singlet exciton fission photovoltaics. *Accounts of Chemical Research* **46**, 1300–1311 (2013). PMID: 23611026.

[5] Pandey, A. K. Highly efficient spin-conversion effect leading to energy up-converted electroluminescence in singlet fission photovoltaics. *Sci. Rep.* **5** (2015).

[6] Tang, C. W. & VanSlyke, S. A. Organic electroluminescent diodes. *Applied Physics Letters* **51**, 913–915 (1987).

[7] Burroughes, J. H. *et al.* Light-emitting diodes based on conjugated polymers. *Nature* **347**, 539–541 (1990).

[8] Podzorov, V., Pudalov, V. & Gershenson, M. Field-effect transistors on rubrene single crystals with parylene gate insulator. *Appl. Phys. Lett.* **82**, 1739 – 41 (2003).

[9] Takahashi, T., Takenobu, T., Takeya, J. & Iwasa, Y. Ambipolar organic field-effect transistors based on rubrene single crystals. *Applied Physics Letters* **88**, – (2006).

[10] Hecht, E. *Optics* (Addison-Wesley, 2002).

[11] Biaggio, I. Degenerate four-wave mixing in noncentrosymmetric materials. *Phys. Rev. A* **64**, 063813 (2001).

[12] Kogelnik, H. Coupled wave theory for thick hologram gratings. *Bell System Technical Journal* **48**, 2909–2947 (1969).

[13] Beels, M. T., Biaggio, I., Reekie, T., Chiu, M. & Diederich, F. m. c. Two-photon absorption and spectroscopy of the lowest two-photon transition in small donor-acceptor˘substituted organic molecules. *Phys. Rev. A* **91**, 043818 (2015).

[14] Salcedo, J. & Siegman, A. E. Laser induced photoacoustic grating effects in molecular crystals. *Quantum Electronics, IEEE Journal of* **15**, 250–256 (1979).

[15] Nelson, K. A., Lutz, D. R., Fayer, M. D. & Madison, L. Laser-induced phonon spectroscopy. optical generation of ultrasonic waves and investigation of electronic excited-state interactions in solids. *Phys. Rev. B* **24**, 3261–3275 (1981).

[16] Moharam, M. G. & Young, L. Criterion for bragg and raman-nath diffraction regimes. *Appl. Opt.* **17**, 1757–1759 (1978).

[17] Gaylord, T. K. & Moharam, M. G. Thin and thick gratings: terminology clarification. *Appl. Opt.* **20**, 3271–3273 (1981).

[18] Klein, W. & Cook, B. Unified approach to ultrasonic light diffraction. *Sonics and Ultrasonics, IEEE Transactions on* **14**, 123–134 (1967).

[19] Rose, T. S., Righini, R. & Fayer, M. D. Picosecond transient grating measurements of singlet exciton transport in anthracene single crystals. *Chemical Physics Letters* **106**, 13–19 (1984).

[20] Regmi, A., Ganjoo, A., Zhao, D., Jain, H. & Biaggio, I. Fast excited state diffusion in a-as2se3 chalcogenide films. *Applied Physics Letters* **101**, – (2012).

[21] Scharber, M. & Sariciftci, N. Efficiency of bulk-heterojunction organic solar cells. *Progress in Polymer Science* **38**, 1929 – 1940 (2013). Topical issue on Conductive Polymers.

[22] Nakashima, T. T. & Offen, H. W. Crystal spectra of tetracene and rubrene under pressure. *The Journal of Chemical Physics* **48**, 4817–4821 (1968).

[23] Yildiz, A., Kissinger, P. T. & Reilley, C. N. Triplet-triplet fluorescence of rubrene in solution. *The Journal of Chemical Physics* **49**, 1403–1406 (1968).

[24] Pope, M. & Swenberg, C. *Electronic Processes in Organic Crystals and Polymers* (Oxford University Press, 1999).

[25] Eisberg, R. & Resnick, R. *Quantum physics of atoms, molecules, solids, nuclei, and particles*. Quantum Physics of Atoms, Molecules, Solids, Nuclei and Particles (Wiley, 1985).

[26] McGlynn, S. & Azumi, T. *Molecular spectroscopy of the triplet state*. Prentice-Hall international series in chemistry (Prentice-Hall, 1969).

[27] Rao, A. *et al.* Exciton fission and charge generation via triplet excitons in pentacene/c60 bilayers. *Journal of the American Chemical Society* **132**, 12698–12703 (2010). PMID: 20735067.

[28] Smith, M. & Michl, J. Singlet fission. *Chem Rev* **110**, 6891–936 (2010).

[29] Müller, A. M., Avlasevich, Y. S., Schoeller, W. W., Müllen, K. & Bardeen, C. J. Exciton fission and fusion in bis(tetracene) molecules with different covalent linker structures. *Journal of the American Chemical Society* **129**, 14240–14250 (2007). PMID: 17958421.

[30] Chabr, M., Wild, U., Funfschilling, J. & Zschokke-Granacher, I. Quantum beats of prompt fluorescence in tetracene crystals. *Chemical Physics* **57**, 425–430 (1981).

[31] Burdett, J. J. & Bardeen, C. J. Quantum beats in crystalline tetracene delayed fluorescence due to triplet pair coherences produced by direct singlet fission. *Journal of the American Chemical Society* **134**, 8597–8607 (2012).

[32] Tao, S. *et al.* Relaxation dynamics of photoexcited excitons in rubrene single crystals using femtosecond absorption spectroscopy. *Phys. Rev. Lett.* **109**, 097403 (2012).

[33] Ma, L. *et al.* Singlet fission in rubrene single crystal: direct observation by femtosecond pump-probe spectroscopy. *Phys. Chem. Chem. Phys.* **14**, 8307–8312 (2012).

[34] Podzorov, V. *et al.* Intrinsic charge transport on the surface of organic semiconductors. *Phys. Rev. Lett.* **93**, 086602 (2004).

[35] Podzorov, V. & Gershenson, M. Photoinduced charge transfer across the interface between organic molecular crystals and polymers. *Phys. Rev. Lett.* **95**, 016602 – 1 (2005).

[36] Sundar, V. C. *et al.* Elastomeric transistor stamps: Reversible probing of charge transport in organic crystals. *Science* **303**, 1644–1646 (2004).

[37] Irkhin, P. & Biaggio, I. Direct imaging of anisotropic exciton diffusion and triplet diffusion length in rubrene single crystals. *Phys. Rev. Lett.* **107**, 017402 (2011).

[38] Ryasnyanskiy, A. & Biaggio, I. Triplet exciton dynamics in rubrene single crystals. *Phys. Rev. B* **84**, 193203 (2011).

[39] Biaggio, I. Short-pulse induced photocurrent and photoluminescence in organic materials. In Ostroverkhova, O. (ed.) *Handbook of organic materials for optical*

and (opto)electronic devices: Properties and applications, chap. 12, 356–376 (Woodhead Publishing Ltd., 2013).

[40] Biaggio, I. & Irkhin, P. Extremely efficient exciton fission and fusion and its dominant contribution to the photoluminescence yield in rubrene single crystals. *Applied Physics Letters* **103**, – (2013).

[41] Najafov, H., Lyu, B., Biaggio, I. & Podzorov, V. Investigating the origin of the high photoconductivity of rubrene single crystals. *Phys. Rev. B* **77**, 125202 (2008).

[42] Najafov, H., Lyu, B., Biaggio, I. & Podzorov, V. Two mechanisms of exciton dissociation in rubrene single crystals. *Applied Physics Letters* **96**, 183302 (2010).

[43] Irkhin, P., Ryasnyanskiy, A., Koehler, M. & Biaggio, I. Absorption and photoluminescence spectroscopy of rubrene single crystals. *Phys. Rev. B* **86**, 085143 (2012).

[44] Lim, S.-H., Bjorklund, T. G., Spano, F. C. & Bardeen, C. J. Exciton delocalization and superradiance in tetracene thin films and nanoaggregates. *Phys. Rev. Lett.* **92**, 107402 (2004).

[45] Da Silva Filho, D. A., Kim, E.-G. & Bredas, J.-L. Transport properties in the rubrene crystal: Electronic coupling and vibrational reorganization energy. *Advanced Materials* **17**, 1072 – 1076 (2005).

[46] Tao, S. *et al.* Optical pump-probe spectroscopy of photocarriers in rubrene single crystals. *Phys. Rev. B* **83**, 075204 (2011).

[47] Saeki, A., Seki, S., Takenobu, T., Iwasa, Y. & Tagawa, S. Mobility and dynamics of charge carriers in rubrene single crystals studied by flash-photolysis microwave conductivity and optical spectroscopy. *Advanced Materials* **20**, 920–923 (2008).

[48] Xia, Y., Kalihari, V., Frisbie, C. D., Oh, N. K. & Rogers, J. A. Tetracene air-gap single-crystal field-effect transistors. *Appl. Phys. Lett* **90**, 162106 (2007).

[49] El Helou, M., Medenbach, O. & Witte, G. Rubrene microcrystals: A route to investigate surface morphology and bulk anisotropies of organic semiconductors. *Crystal Growth & Design* **10**, 3496–3501 (2010).

[50] Sai, N., Tiago, M. L., Chelikowsky, J. R. & Reboredo, F. A. Optical spectra and exchange-correlation effects in molecular crystals. *Phys. Rev. B* **77**, 161306 (2008).

[51] Monahan, N. & Zhu, X.-Y. Charge transfer–mediated singlet fission. *Annual Review of Physical Chemistry* **66**, 601–618 (2015). PMID: 25648486.

[52] Ma, L. *et al.* Two-photon-induced singlet fission in rubrene single crystal. *J. Chem. Phys. of Chemical Physics* **138**, 184508 (2013).

[53] Marian, C. M. Spin–orbit coupling and intersystem crossing in molecules. *Wiley Interdisciplinary Reviews: Computational Molecular Science* **2**, 187–203 (2012).

[54] Furube, A., Katoh, R., Mitsuta, H., Miyadera, T. & Yoshida, Y. Picosecond multiple exciton generation from the excited singlet state in rubrene single crystal. In *Meeting Abstracts*, 38, 1831–1831 (The Electrochemical Society, 2011).

[55] Jankus, V. *et al.* Competition between polaron pair formation and singlet fission observed in amorphous rubrene films. *Phys. Rev. B* **87**, 224202 (2013).

[56] Piland, G. B., Burdett, J. J., Kurunthu, D. & Bardeen, C. J. Magnetic field effects on singlet fission and fluorescence decay dynamics in amorphous rubrene. *The Journal of Physical Chemistry C* **117**, 1224–1236 (2013).

[57] Kepler, C. & Avakian, A. Triplet excitons and delayed fluorescence in anthracene crystals. *Phys. Rev. Lett.* **10** (1963).

[58] Hall, J. L., Jennings, D. A. & McClintock, R. M. Study of anthracene fluorescence excited by the ruby giant-pulse laser. *Phys. Rev. Lett.* **11**, 364–366 (1963).

[59] Darmanyan, A. P. Nature of lasting luminescence of rubrene in solution. *Russian Chemical Bulletin* **31**, 1679–1682 (1982). 10.1007/BF00956909.

[60] Nelson, K. A., Lutz, D., Fayer, M. & Madison, L. Laser-induced phonon spectroscopy, optical generation of ultrasonic waves and investigation of electronic excited-state interactions in solids. *Phys. Rev. B* **24**, 3261–3275 (1981).

[61] Nelson, K. A., Miller, R. D., Lutz, D. & Fayer, M. Optical generation of tunable ultrasonic waves. *Journal of Applied Physics* **53**, 1144 – 1149 (1982).

[62] Weinberg-Wolf, J., McNeil, L., Liu, S. & Kloc, C. Evidence of low intermolecular coupling in rubrene single crystals by raman scattering. *Journal of Physics. Condensed Matter* **19**, 276204 (2007).

[63] Petrenko, T., Krylova, O., Neese, F. & Sokolowski, M. Optical absorption and emission properties of rubrene: insight from a combined experimental and theoretical study. *New Journal of Physics* **11** (2007).

Kanimambo ao Todo Mundo!

Special thanks to Professor Biaggio for all your help, guidance, and teaching throughout the years. Mostly, thanks for minimally chastising me when I would shirk research responsibilities for teaching.

Many thanks to Lois and Pam for keeping the department running; to Rich and Wayne for helping me be a good TA; to John for making my experiments easier.

I appreciate the helpful talks and encouragement provided by my committee members: Drs. Huennekens, Rotkin, Stavola, and Strandwitz.

Thanks to Drs. Licini, De Leo and Stavola for helping me grow as an educator.

Thanks to Dr. Vitaly Podzorov of Rutgers Univ. for providing rubrene crystals.

Thanks to group members past and present. In particular: Dr. Marten Beels for teaching me how to be a grad student. Britney Richman for taking excellent data. Vinnie Zoutenbier for obtaining the PL spectra and images of my samples, and for keeping it fun both in and out of the lab.

Thanks to the Lehigh farming community for all the friendship, learning and food you have provided.

Finally, a deep love to my family and friends. Daniel, photographer of rubrene, grower of food, maker of music and cocktails and all that is good in life. Thank you my love. Mom and Dad, thank you for your love, for teaching me, well, everything, and for your *constant* encouragement. Thank you to the most amazing and compassionate woman I know, my sister Kyla. Thanks to Rita and Björn for all your support. Thanks to The Crwo for the continuous stream of shenanigans. Thanks to The Girls for inspiring me in everything you do, particularly Jess for the various liquid and solid ways you supplied encouragement.

Vita

Kebra Ann Ward completed her undergraduate studies at the University of Southern California with a B.S. in astronomy in 2004. From 2005-2007 she served as a Peace Corps Volunteer in the south African country of Moçambique as a high school biology teacher. In 2010 she began her graduate studies at Lehigh University, where she was awarded a Master's degree in Physics in January of 2012, and her PhD in Physics in August of 2015.